STARS

Electronic Theses and Dissertations, 2020-

2020

High Performance Micro-scale Light Emitting Diode Display

Fangwang Gou
University of Central Florida

Find similar works at: https://stars.library.ucf.edu/etd2020

University of Central Florida Libraries http://library.ucf.edu

STARS Citation

Showcase of Text, Archives, Research & Scholarship

HIGH-PERFORMANCE MICRO-SCALE LIGHT EMITTING DIODE DISPLAY

by

FANGWANG GOU
B.S. University of Electronic Science and Technology of China, 2012
M.S. Peking University, 2015

A dissertation submitted in partial fulfillment of the requirements
for the degree of Doctor of Philosophy
in the College of Optics and Photonics
at the University of Central Florida
Orlando, Florida

Summer Term
2020

Major Professor: Shin-Tson Wu

ABSTRACT

Micro-scale light emitting diode (micro-LED) is a potentially disruptive display technology because of its outstanding features such as high dynamic range, good sunlight readability, long lifetime, low power consumption, and wide color gamut. To achieve full-color displays, three approaches are commonly used: 1) to assemble individual RGB micro-LED pixels from semiconductor wafers to the same driving backplane through pick-and-place approach, which is referred to as mass transfer process; 2) to utilize monochromatic blue micro-LED with a color conversion film to obtain a white source first, and then employ color filters to form RGB pixels, and 3) to use blue or ultraviolet (UV) micro-LEDs to pump pixelated quantum dots (QDs). This dissertation is devoted to investigating and improving optical performance of these three types of micro-LED displays from device design viewpoints.

For RGB micro-LED display, angular color shift may become visually noticeable due to mismatched angular distributions between AlGaInP-based red micro-LED and InGaN-based blue/green counterparts. Based on our simulations and experiments, we find that the mismatched angular distributions are caused by sidewall emission from RGB micro-LEDs. To address this issue, we propose a device structure with top black matrix and taper angle in micro-LEDs, which greatly suppresses the color shift while keeping a reasonably high light extraction efficiency. These findings will shed new light to guide future micro-LED display designs.

For white micro-LEDs, the color filters would absorb 2/3 of the outgoing light, which increases power consumption. In addition, color crosstalk would occur due to scattering of the color conversion layer. With funnel-tube array and reflective coating on its inner surface, the crosstalk is eliminated and the optical efficiency is enhanced by ~3X.

For quantum dot-converted micro-LED display, its ambient contrast ratio degrades because the top QD converter can be excited by the ambient light. To solve this issue, we build a verified simulation model to quantitatively analyze the ambient reflection of quantum dot-converted micro-LED system and improve its ambient contrast ratio with a top color filter layer.

To my beloved family.

ACKNOWLEDGMENTS

Five-year Ph.D. study is a challenging and yet enjoyable experience for me. It would not be possible without the support from those around me. I hold my sincere gratitude towards my advisor, Prof. Shin-Tson Wu, for his inspirational guidance, continuous encouragement, and strong support. He will be my lifelong role model of a scientist and teacher. I would also like to thank Prof. Wu's better half, our beloved Shimu, Cho-Yan Hiseh, for her love over the years.

I am thankful to my committee members, Prof. M. G. Moharam, Prof. Patrick L. LiKamWa, late Prof. Boris Y. Zeldovich, and Prof. Yajie Dong. They have been always supportive in supervising my research and providing strong recommendations for my society award applications.

I would like to thank our senior fellow group members, Dr. Ruidong Zhu, Dr. Fenglin Peng, Dr. Haiwei Chen, Dr. Yun-Han Lee, Dr. Guanjun Tan and Dr. Juan He, for helping me understand physical simulations and teaching me to do experiments. I would also like to thank Dr. Yuge Huang, Tao Zhan, Ziqian He, Kun Yin, Jianghao Xiong, En-Lin Hsiang, Junyu Zou, Yannanqi Li, Zhiyong Yang and Qian Yang for many valuable discussions and suggestions.

I appreciate the help and support from Victor Yin, Mark Son, Dr. Yi-Pai Huang, Dr. Jun Qi, Dr. Zhibing Ge, David Suh, Darren So, Dr. Daming Xu, Dr. Yufeng Yan and Dr. Hao Chen at Apple Inc. during my internship.

Lastly, I would like to thank my parents, my parents-in-law, and my brother, for their care and love. And most of all, I would like to thank my husband, Ji Chen, for being my rock throughout all the ups and downs. It is his unconditional love that gives me courage and keeps me moving forward.

TABLE OF CONTENTS

LIST OF FIGURES

LIST OF TABLES

CHAPTER 1 : INTRODUCTION

III-nitride-based light emitting diodes (LEDs) have been widely used for various applications such as lighting [1], signal [2], visible light communication [3,4] and displays [5,6] owing to the fact that they are reliable and high efficient solid-state light sources. For conventional LEDs with chip size lager than 200 μm × 200 μm, they provide sufficient brightness for backlighting [7] in liquid crystal displays (LCDs) [8] and outdoor or indoor public displays. As the improvement of manufacturing capability, the LED chip size is reduced to between 100 μm to 200 μm, which is called mini-LED [9,10]. It has been widely used as direct-lit backlight for LCDs with local dimming technology [11–13] to achieve high dynamic range. However, as the increasing demand of high-resolution displays including mobile phones, head-mounted devices and wearable displays, it requires to further miniaturize the LED chip size to be less than 100 μm × 100 μm, which is referred to as micro-scale LED (micro-LED) [14–16].

1.1 Basis of Micro-LED

Nowadays, LCD and organic light emitting diode (OLED) [17] are dominant display technologies in the market. For traditional LCD, it consists of LED backlight system, aligned liquid crystal as light switch, polarizers, optical compensation film stack and color filter array to form red, green, and blue (RGB) subpixels. Although various techniques, including quantum-dot color-conversion film [18,19], local dimming, new LC materials [20] and modes [21], have been proposed to improve the performance of LCD in terms of wide color gamut, high dynamic range and faster response time, it still has limitation in optical efficiency (only ~5%). Different from LCDs, OLED is self-emissive and each pixel can be switched on and off individually, which

enables a true black state. However, it suffers from low brightness and limited lifetime due to its organic nature. Compared to LCD and OLED, micro-LED is a potentially disruptive display technology because of its outstanding features such as nanosecond response time, high dynamic range, low power consumption, and long lifetime [22–24].

Table 1-1 Comparisons of LCD, OLED and micro-LED displays.

	LCD	OLED	Micro-LED
Light efficiency	Low	Medium	High
Peak brightness	Medium	Low	High
Contrast ratio	1000:1	1000,000:1	1000,000:1
Response time	3 ms	μs	ns
MPRT [25,26] (90Hz, 0.1 duty ratio)	1 ms	1 ms	1 ms
Image retention	No	Yes	No
Temperature range	-40°C ~ 100°C	-50°C ~ 70°C	-100°C ~ 120°C
Lifetime	>10 years	~3 years	>10 years
Cost	Low	Medium	High

The investigations of micro-LED start from the early 2000s and it has been proved to have higher light extraction efficiency, better current spreading and lower self-heating effect compared to traditional LEDs [27,28]. In recent years, more and more companies have established programs in micro-LED technology. For example, Sony launched its first 55 inch "Crystal LED" display with a resolution of 1920×1080 in 2012, which consists of about 6 million micro LEDs. In 2017,

Sony released the "Crystal LED Display System" with micro-LED chip size of only ~20 µm and pixel pitch of 1.26 mm [29]. The emitting area is only ~1% and the rest 99% area are black, which enables high contrast ratio even in a bright environment. In addition, the emission patterns of RGB micro-LEDs are very close to *Lambertian* distribution and are well matched, leading to a wide viewing angle. In 2018, AU Optronics Corp. demonstrated a 12.1 inch full-color micro-LED display with a resolution of 169 pixel per inch (PPI) by utilizing blue micro-LED with chip size less than 30 µm to pump red and green color conversion materials [30]. PlayNitride has demonstrated a 114 PPI transparent "PixeLED" micro-LED display with a transparency of ~60% based on an active driven LTPS backplane [31]. PlayNitride has also demonstrated a 468 PPI wearable micro-LED device and a flexible micro-LED display with thickness of only 28 µm. In 2019, Jade Bird Display (JBD) presented a 600 DPI (dots per inch) bi-color Micro-LED display which implanted JBD's proprietary transferring technology to assemble red and green chips to silicon CMOS backplane. Also, JBD exhibited a mono-color Micro-LED module with a pitch size of only 2.5 µm and a resolution of 10,000 DPI. It achieved a very high brightness of million nits, which has potential applications in augmented reality (AR). X-Celeprint has demonstrated a 5.1-inch, 70 PPI Micro-LED display which was made of 8 × 15 µm RGB chips based on active driven Micro IC [32]. glō Inc. has demonstrated a 0.7 inch micro-LED display with 1000 PPI and a brightness of 100,000 nits achieved by GaN nanowires technology. Compared to planar micro-LEDs in which efficiency decreases as chip size shrinks, the efficiency of nanowire micro-LED improves with decreasing size, which greatly saves the power consumption.

To assemble a micro-LED display, two major processes have been proposed. The first one is mass transfer, which assembles individual RGB micro-LED pixels from semiconductor wafers

to the same driving backplane through pick-and-place approach [33–36]. This approach requires precise alignment for each pixel and can be used for building of middle- and large-sized displays including mobile phone, monitor, TV or video wall. The second method is monolithic integration [37–39], which includes growth of micro-LED chips on a single epitaxial wafer and bonding with driving circuit. This method is only ideal for small sized displays such as smart watches and micro-projectors due to the limitation of wafer size for growth of LEDs (usually 4~8 inches) [40,41].

1.2 Challenges and Motivations

Although the science is clear, micro-LED still faces many technical challenges as the chip size shrinks. For example, to reduce the manufacturing cost, larger-sized epitaxial wafers with wavelength uniformity are necessary [42]. In addition, it requires that the yield of mass transfer process reaches to 99.99% to let the following defect testing and repairing become manageable. In terms of driving, it is still under debating that which technique including CMOS diver IC or thin-film transistor (TFT) is more suitable. Another challenge is full-color formation. Figure 1-1 shows the layout of three typical color formation approaches: (a) assemble RGB subpixels with individual RGB micro-LED chips through mass transfer process; (b) utilize monochromatic blue micro-LED with a color conversion film to obtain white source first, and then employ color filters to form RGB pixels [43,44], which is referred to as white micro-LED in this dissertation; (c) use blue or ultraviolet (UV) micro-LEDs to pump pixelated RG or RGB quantum dots [45,46].

4

(a)

Substrate

| R | G | B |

Substrate

(b)

Substrate

CF | CF | CF

QD / Phosphor

| B | B | B |

Substrate

(c)

Substrate

QD | QD

| B | B | B |

Substrate
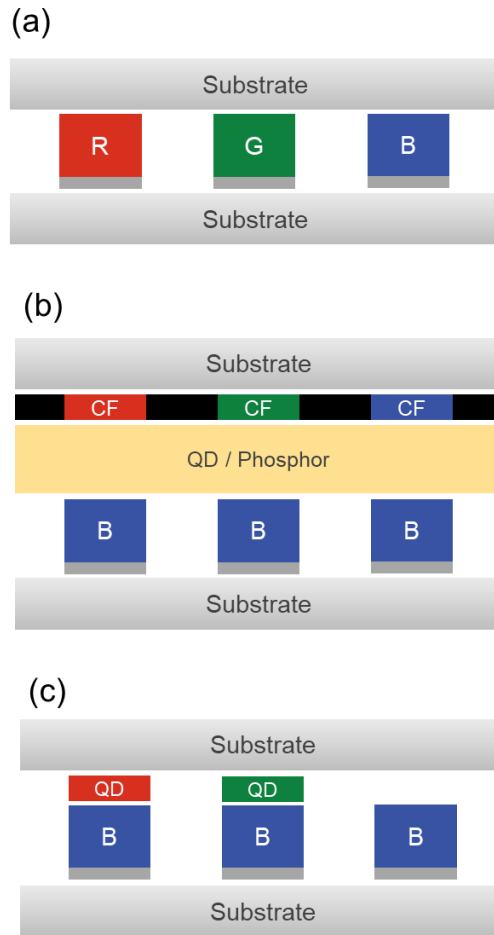
Figure 1-1 Schematic layout of full-color micro-LED displays. (a) RGB micro-LED; (b) White micro-LED; (c) QD-converted micro-LED.

However, for each full-color formation approach, many issues arise as listed as below:

1) For full-color micro-LED display consists of individual RGB LED chips, as the chip size down to micron scale, although the internal quantum efficiency may droop due to increased non-radiative recombination from sidewall defects, its light extraction efficiency is improved because the light emission from sidewall gradually increases [47–51]. However, the far-field radiation pattern would deviate from ideal *Lambertian* distribution, depending on the sidewall emission intensity, which is

5

determined by the refractive index of the employed semiconductor material and device structure. For commercial LEDs, the most commonly used epitaxy wafer for red LED is based on GaInP/AlGaInP multi-quantum wells (MQWs), while blue and green LEDs are based on InGaN/GaN MQWs [52,53]. Therefore, angular distribution mismatch among RGB micro-LEDs would occur because the red chip uses different epitaxy materials and has different structures from the green and blue ones. As a result, the angular color shift of mixed colors, such as skin tone, by mixing RGB colors with different ratios may become distinguishable by the human eye [54].

2) For white micro-LEDs, it only needs one type of LED epitaxy wafer and the color down-conversion layer does not need to be pixelated, which is more feasible for manufacturing. However, the color filters would absorb 2/3 of the outgoing light, which increases power consumption. In addition, color crosstalk would occur due to scattering of the color conversion layer.

3) For QD-converted micro-LED, it can achieve a wide color gamut since QDs have narrow photo-luminescent emission spectra [55–57]. Moreover, it does not need color filters compared to white micro-LED, which enables a higher optical efficiency. However, for complete color down-conversion, the optical density (OD) of the QDs resin layer must be high, which requires highly absorbing QDs and a relatively thick layer. Therefore, distributed Bragg reflector is needed to recycle the blue or UV light to improve the light conversion efficiency. A drawback of this approach is the degraded ambient contrast ratio. In addition, the top QD layer can be excited not only by the light from the micro-LED, but also by the short-wavelength component of the ambient light,

which will degrade the ambient contrast ratio of the displays [58]. Therefore, how to analyze the ambient excitation of QDs quantitatively needs to be explored.

This dissertation will mainly focus on possible solutions to above-mentioned challenges for these three types of micro-LED displays. In Chapter 2, the angular color shift and light extraction efficiency of RGB individual micro-LEDs are investigated. In Chapter 3, a funnel-tube array is proposed to eliminate color crosstalk and triple the optical efficiency in white micro-LEDs. In Chapter 4, the ambient excitation of color-converted micro-LED is analyzed quantitatively.

CHAPTER 2 : RGB MICRO-LED

2.1 Background

The most straightforward approach to achieve full-color micro-LED display is to assemble individual RGB micro-LED pixels from semiconductor wafers to the same driving backplane through pick-and-place approach, which is referred to as mass transfer process. Although it is still challenging to achieve high manufacturing yield with low cost, large-size displays consisting of full-color micro-LED modules are emerging, such as Sony Crystal-LED TVs, Samsung micro-LED video walls and so on.

To fabricate micro-LEDs, III-nitride materials have been proved to be excellent candidates to achieve high efficiency and high power [59,60]. Although III-nitride materials are considered to be monochromatic emission sources, in theory, RGB colors can be generated by tuning the indium composition in the InGaN/GaN multiple quantum wells (MQWs). However, the luminescence efficiency of InGaN-based red LED are still low due to large lattice mismatch between the InGaN active layer and GaN buffer for red wavelength. As a results, high efficiency full-color micro-LED displays cannot be achieved with GaN family alone. Instead, AlGaInP-based micro-LED has been commonly employed for red emission [61].

For a micro-LED, as the chip size down to micron scale, although the internal quantum efficiency may droop due to increased non-radiative recombination from sidewall defects [48,62], its light extraction efficiency is improved because the light emission from sidewall gradually increases [63]. However, the far-field radiation pattern would deviate from ideal *Lambertian* distribution, depending on the sidewall emission intensity, which is determined by the refractive index of the employed semiconductor material and device structure. For full-color micro-LEDs,

because the epitaxy wafer for red LED is based on GaInP/AlGaInP MQWs, while blue and green LEDs are based on InGaN/GaN MQWs, angular distribution mismatch among RGB micro-LEDs would occur. As a result, the angular color shift of mixed colors, such as skin tone, by mixing RGB colors with different ratios may become distinguishable by the human eye.

2.2 Simulation Model and Experiment

Table 2-1 Optical parameters of commonly used AlGaInP-based red micro-LED and InGaN-based blue and green micro-LEDs adopted in simulations.

Red Layers	Thickness (μm)	n	k	Green/Blue Layers	Thickness (μm)	n		k	
						Green	Blue	Green	Blue
ITO	0.1	2.07	0	n-GaN	2.5	2.38	2.43	4e-5	4e-5
p-GaP	1.0	3.33	0	MQW	0.1	2.41	2.49	2e-2	2e-2
p-AlGaInP	0.1	3.30	0	p-AlGaN	0.05	2.31	2.35	6e-4	7e-4
p-AlInP	0.6	3.21	0	p-GaN	0.3	2.38	2.43	4e-5	4e-5
MQW	0.4	3.60	0.16	n/p-Metal	0.5	0.44	1.43	2.29	1.85
n-AlInP	0.3	3.21	0	-	-	-	-	-	-
n-AlGaInP	1.2	3.30	0	-	-	-	-	-	-
n/p-Metal	0.5	0.15	3.52	-	-	-	-	-	-

In order to analyze the color shift of RGB micro-LED displays originated from mismatched angular distribution, firstly we need to examine the emission patterns of RGB micro-LEDs at different viewing angles. We build a simulation model with ray-tracing software LightTools. Table 2-1 lists the commonly used major structure layers and their thicknesses of flip-chip RGB chips.

9

For AlGaInP-based red micro-LED, it consists of metal contact layer, n-cladding AlGaInP, n-type AlInP diffusion barrier, GaInP/AlGaInP MQWs, p-type AlInP diffusion barrier, p-cladding AlGaInP, and p-GaP window layer [61]. For InGaN-based green and blue micro-LEDs, their structures have metal contact layer, p-type GaN, AlGaN electron block layer, InGaN/GaN MQWs and n-type GaN. Although only the refractive indices at central wavelength are included in Table 2-1, the wavelength dispersion of refractive index for each material (Fig. 2-1) is also considered in our simulation [64,65]. The die sizes are all 35 × 60 μm in order to be comparable to some commercial products. For simplicity, the metal pad is set to be the same size as chip size. The layout and materials of blue and green micro-LED are similar, but they are quite different from those of red chip. Light radiation from the multi-quantum wells (MQWs) with uniform angular distribution travels through each layer and across interfaces according to Snell's law.
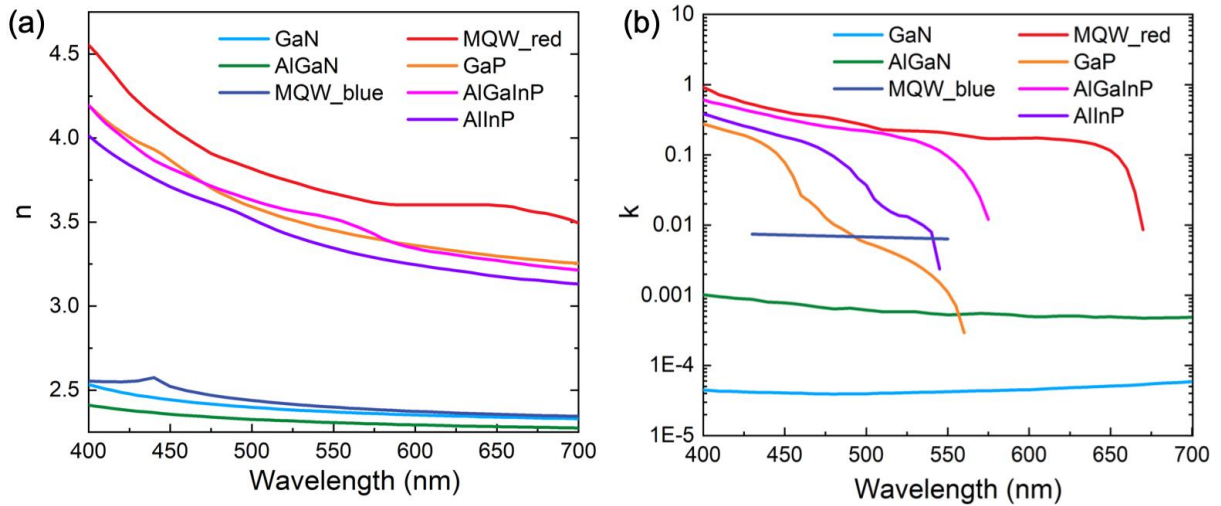
Figure 2-1 Refractive indexes of RGB micro-LED epitaxial material.

2.3 Emission Spectra and Angular Distributions

To validate our model, RGB micro-LEDs with the same chip size 35×60 µm are fabricated (Fig. 2-2). The measured emission spectra of RGB chips from normal direction to 60° viewing angle are plotted in Fig. 2-3. For each device, the central wavelength does not shift as viewing angle increases, indicating the cavity effect inside micro-LEDs is negligible. The central wavelength and full width at half maximum (FWHM) for RGB chips are [626 nm, 14 nm] for red, [529 nm, 34 nm] for green, and [465 nm, 16 nm] for blue. It should be mentioned here that organic LED intentionally utilizes the cavity effect to narrow the emission spectra, but the tradeoff is noticeable color shift [54].
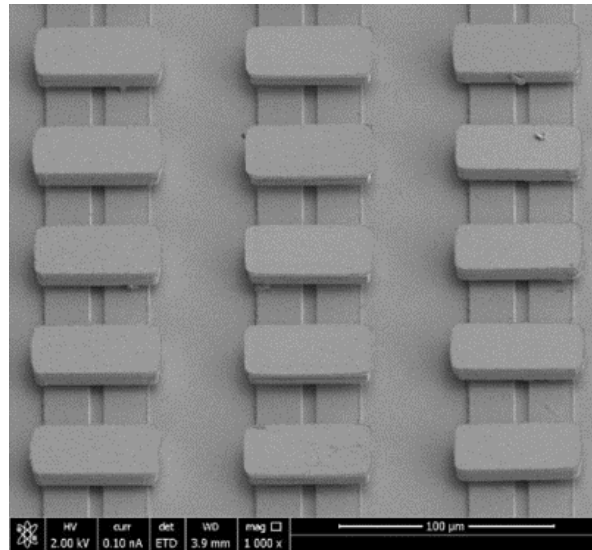
Figure 2-2 SEM image of RGB micro-LEDs arrays after transfer.
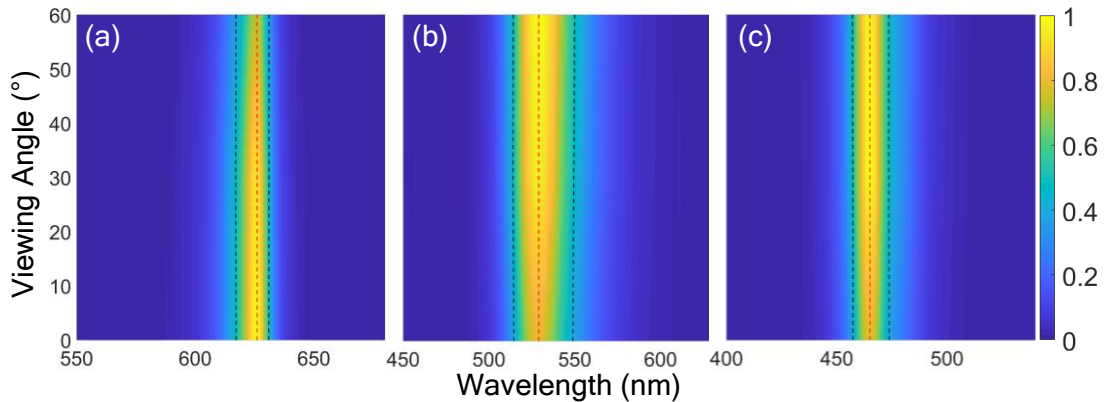
Figure 2-3 Measured emission spectra of (a) red, (b) green, and (c) blue micro-LEDs at different viewing angles. Red and black dashed lines indicate the central wavelength and FWHM at each viewing angle.

Figure 2-4 shows the far-field radiation patterns of our RGB micro-LEDs. Dots represent the measured data and solid lines stand for simulation results. As can be seen, good agreement between experiment and simulation is obtained. As viewing angle increases, the light emission from red chip declines following Lambert's cosine law. In contrast, for green and blue micro-LEDs, the light intensity gets stronger from normal angle to ~40° and then decreases. The mismatched angular distributions originate from different materials of RGB chips and will cause angular color shift of mixed colors.
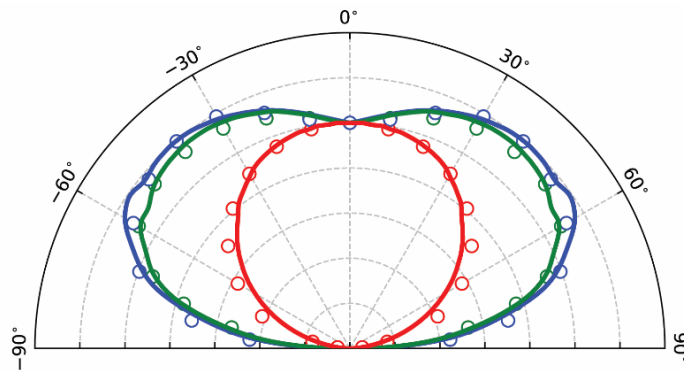
Figure 2-4 Far-field radiation patterns of RGB micro-LEDs. Dots are experimental data and lines are simulation results.

For a traditional LED with chip size at millimeter scale, the light emission from top surface dominates, which is limited by total internal reflection. The critical angle (θ_c) between the semiconductor and air interface determines the amount of light escaping from LED and it can be calculated according to Snell's Law:

$$\theta_c = \sin^{-1}(\frac{n_{air}}{n}).$$ (1)

In Eq. (1), n_{air} and n represents the refractive index of the air and top semiconductor layer, respectively. If we neglect the Fresnel loss at semiconductor/air interface, the light extraction efficiency η of the LED can be estimated using following equation [66]:

$$\eta = \frac{\Omega}{4\pi},$$ (2)

where Ω is the solid angle of escape cone, which is expressed as:

$$\Omega = \int_0^{2\pi} d\phi \int_0^{\theta_c} \sin\theta d\theta.$$ (3)

However, as the chip size shrinks, the sidewall emission from micro-LED should also be taken into consideration. In other words, after photons are generated from the MQWs, they can be extracted from all of six surfaces of the chip. Figure 2-5 depict the simulated top and sidewall emissions from RGB micro-LEDs. As can be seen, the top emissions of RGB chips are all *Lambertian* distributions, but the sidewall emission from green and blue chips are much stronger than that from red one. This difference originates from the stronger absorption of red MQW than that of green and blue MQWs.
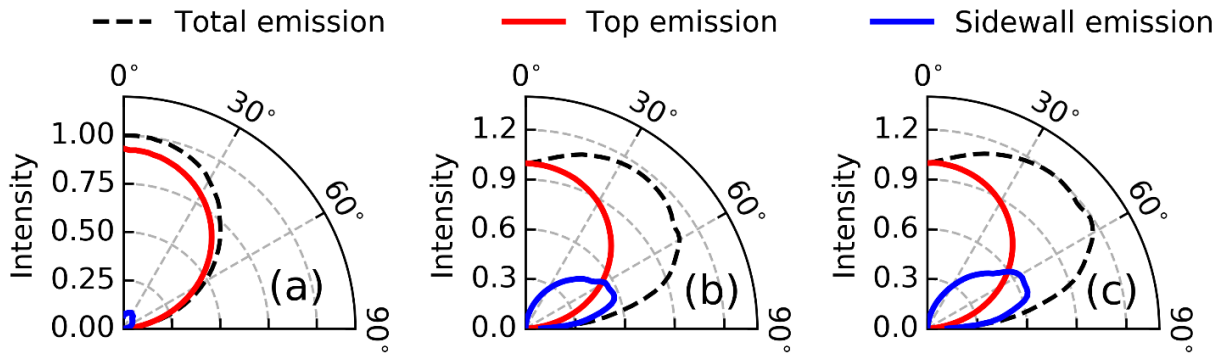
Figure 2-5 Simulated total, top and sidewall emissions of (a) red, (b) green, and (c) blue micro-LEDs at different viewing angles.
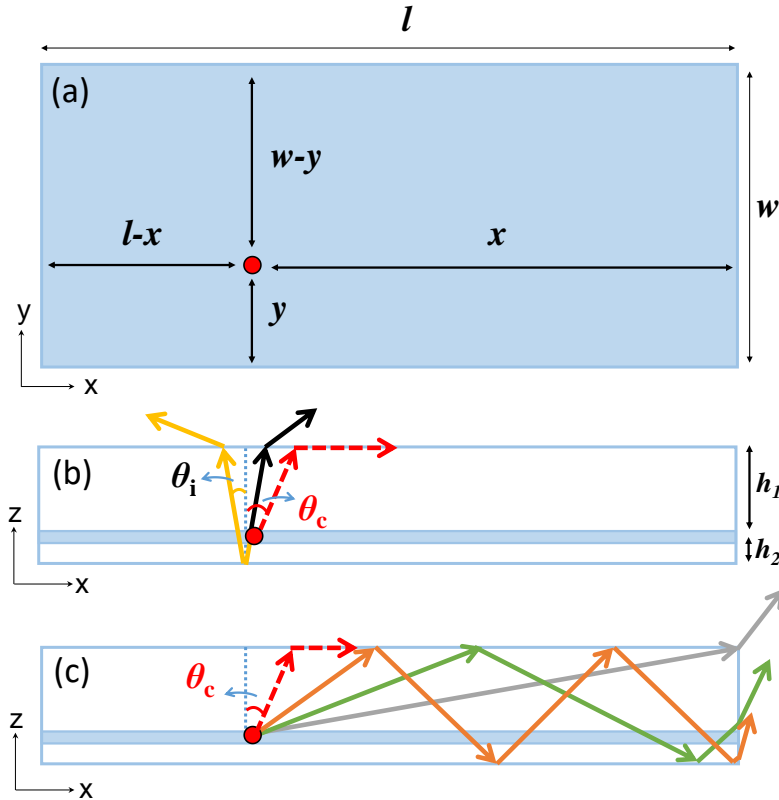
Figure 2-6 (a) Top view of micro-LED chip with a point-like source located at (x, y). (b, c) Side views of light emission from the point source with emission angle θ_i: (a) $\theta_i < \theta_c$: top emission; (c) $\theta_i > 90° - \theta_c$: sidewall emissions.

To analyze the light path inside the micro-LED, we take a point-like source located at MQW layer with coordinate (x, y) as an example (Fig. 2-6(a)). The chip size is $l \times w$ and the

distance of MQW from top surface is h1. On the top surface, the light can be extracted for the rays with θi smaller than θc, as depicted by the black line in Fig. 2-6(b). We can obtain a completed escape cone due to the short distance h1 between MQW and the semiconductor/air interface. The top emission ratio to the total emission intensity can be calculated using Eq. (3). In the opposite direction, the light goes downward and gets reflected by the bottom electrode pad back to top surface [i.e. yellow line in Fig. 2-6 (b)], which should be also included as top emission. But for the downward light, both reflectance Rs of bottom metal pad and absorption of MQW need to be taken into consideration during calculation.

For the emission towards sidewall, the escape cone may not be completed, depending on the position of point-like sources located at the MQW layer. For example, the point source at a short distance from sidewall can get a completed escape cone. However, as the distance increases, the escape cone will become uncompleted because of the small thickness of micro-LED chip ($<$ 4 μm). Fig. 2-6(c) shows the side-view of light emissions from the point source with angle θ_i satisfying $90° - \theta_c < \theta_i < 90°$. Light within this angle range will escape from the sidewall but experience different absorption or reflection losses. For example, when the light emission from the point source reaches the top edge of the sidewall without experiencing reflection [gray line in Fig. 2-6(c)], we can obtain a light escape cone $\theta_1 = \tan^{-1}(h_1/x)$ without absorption and reflection loss. The emission ratio can be calculated using Eqs. (2) and (3). If the emission angle θ_i satisfies $90° - \theta_c < \theta_i < 90° - \theta_1$, although the light can still escape from sidewall, it will experience multiple reflections between top and bottom surfaces as well as absorption of MQW, which are illustrated by green and orange lines in Fig. 2-6(c). For the light reflected by the bottom surface n times, the sidewall emission ratio can be estimated by modifying Eqs. (2) and (3) as:

$$\eta_n = \frac{1}{2} e^{-2n\alpha d} R_s{}^n \int_{\theta_{n-1}}^{\theta_n} \sin\theta d\theta. \qquad (4)$$

In Eq. (4), α and d represent the absorption coefficient and thickness of MQW layer, and R_s is the reflectance of bottom metal pad. For simplicity, we have neglected the Fresnel loss at semiconductor/air interface and the refraction between different layers inside micro-LED. Thus, the total sidewall emission ratio from four side surfaces can be calculated by adding all the ratios together.

Table 2-2 Simulated and calculated sidewall emission ratio for a RGB micro-LED display with different chip size.

Chip size (μm²)	Red		Green		Blue	
	Sim.	Cal.	Sim.	Cal.	Sim.	Cal.
15×30	10.8%	11.0%	58.9%	58.5%	62.2%	65.7%
35×60	5.3%	5.6%	52.4%	54.2%	55.1%	56.7%
50×100	3.8%	4.0%	47.2%	49.6%	50.1%	52.9%

The calculated sidewall emission ratio by MATLAB and the simulated data using ray-tracing in LightTools for micro-LEDs with different chip size are listed in Table 2-2. The agreement between these two methods is very good. As the chip size shrinks from 50×100 μm2 to 15×30 μm2, the sidewall emissions from RGB micro-LEDs increase because of lower absorption and reflection losses inside the chip. For red micro-LEDs, the sidewall emission ratio is much smaller than that from green and blue ones due to stronger absorption of red MQW, resulting in a mismatched angular distribution among RGB micro-LEDs.

2.4 Angular Color Shift

To analyze the color shift induced by subpixels' angular distribution mismatch, a more representative way is to calculate the color shifts of the mixed colors by RGB color mixing. We have defined 10 reference colors in total in order to evaluate color shift throughout the entire color gamut. These reference colors include three primary colors, white point D65, and six mixed colors (three 100% saturated colors and three 50% saturated colors), which are plotted in CIE 1976 color space [67,68] , as shown in Fig. 2-7.
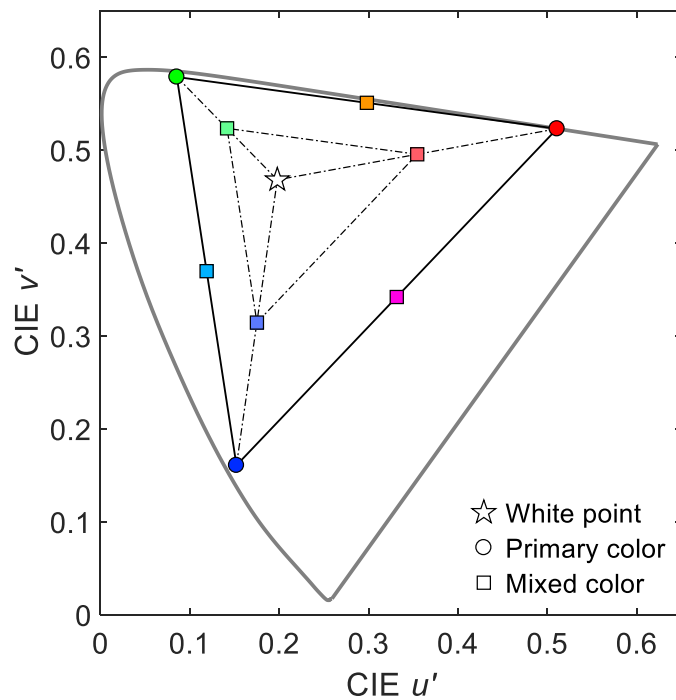
Figure 2-7 10 reference colors in CIE1976 color space, with D65 white point and RGB micro-LEDs primary colors.
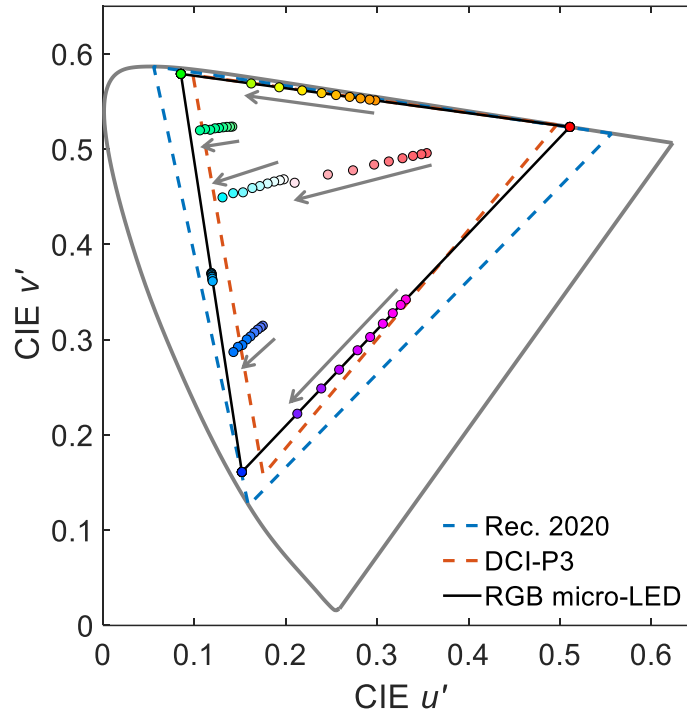
Figure 2-8 Simulated color triangle of the RGB micro-LED display system and the angular color shifts of 10 reference colors from 0° to 80° viewing angle.

Figure 2-8 depicts the color triangle of the RGB micro-LED display and CIE coordinates of 10 reference colors at viewing angles from 0° to 80° with 10° intervals. For primary colors, no color shift is observed at fixed driving current due to weak cavity effect inside micro-LEDs. While for mixed colors and white point, color shift becomes worse as viewing angle increases as expected. The average color shift $\Delta u'v'$ of all colors at 80° is 0.061 and the maximum value is 0.169 for magenta channel, which exceeds the just-noticeable level ($\Delta u'v' < 0.02$). This issue will get worse as the micro-LED size decreases because of increased sidewall emissions from green and blue chips, as listed in Table 2-2. Therefore, it is necessary to improve the color performance of RGB micro-LED display system, especially for high resolution applications.
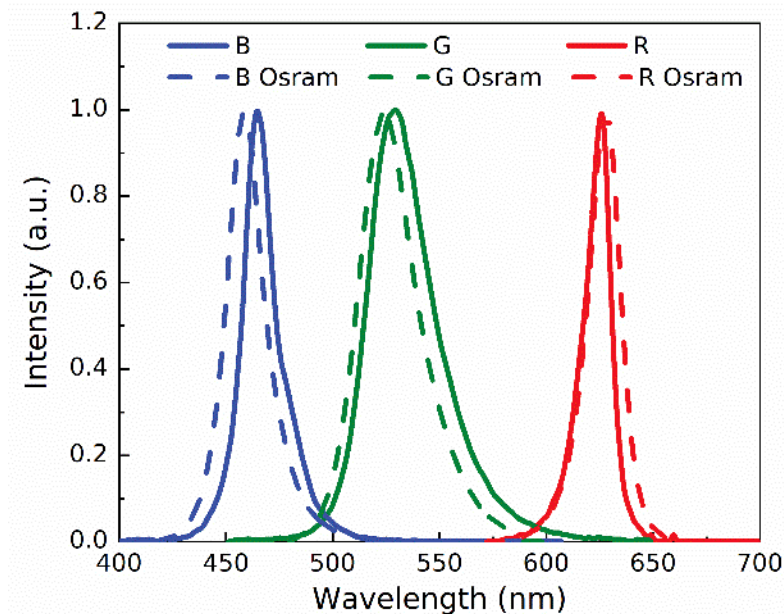
Figure 2-9 RGB spectra of our and Osram's micro-LEDs.

In terms of color gamut, our display device can cover 97% of DCI-P3 standard and 78% of Rec. 2020 standard, as indicated by the color triangle in Fig. 2-8. The relatively narrow color gamut coverage results from the spectral crosstalk between green and red chips, as Fig. 2-9 shows. Compared to our device, the Osram's green LED has a slightly shorter central wavelength and narrower FWHM. As a result, it has less crosstalk with the red LED and its RGB LED system can achieve wider color gamut. The calculated color gamut coverage is 99% of DCI-P3 standard and 90% of Rec.2020 standard. To achieve a desired color gamut, we can tune the electroluminescent (EL) spectrum of green micro-LED by controlling the well/barrier width and indium composition of MQW [69].

To reduce color shift, a straightforward method is to obtain matched RGB radiation patterns, i.e. *Lambertian* distribution, which means the sidewall emissions from green and blue micro-LEDs should be eliminated. Figure 2-10 illustrates our proposed display configuration

consisting of micro-LED array and top black matrix outside the emission region. The gap between micro-LEDs are filled with resin or other dioxide materials with refractive index of ~1.5. As a result, the sidewall emissions from green and blue chips can be completely absorbed by the black matrix, allowing only emissions from top surface of RGB micro-LEDs with matched *Lambertian* distributions. Thus, a negligible color shift can be obtained, but the trade-off is ~2x lower optical efficiency, because the sidewall emission ratios of green and blue chips contribute to ~50% of the total emission intensity, as listed in Table 2-2.
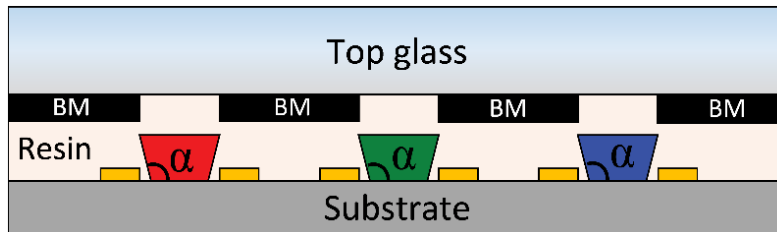
Figure 2-10 RGB micro-LED display with taper angle α and top black matrix.

Since power consumption is another key performance metric for displays, we introduce a taper angle α in the micro-LED structure (Fig. 2-10) to improve the light intensity from top surface [70–72]. The simulated light intensity is normalized to the device with normal angle and without black matrix as Fig. 2-11 shows. As the taper angle α changes from 90° to 140°, the light intensity from green and blue chips first increases and then saturates, while that from red LED almost keeps steady. The color shift becomes severe even if the presence of black matrix when α is larger than 130°. This is because a larger taper angle causes a narrower angular distribution of top emissions for green and blue LEDs but it has little impact on the red counterpart. Thus, the mismatched angular distribution causes a severe color shift. By considering device fabrication, light efficiency as well as color shift, taper angle $\alpha = 120°$ is an optimal choice. With this

configuration, the light efficiency of green and blue micro-LEDs can be boosted to 83% and 86%, respectively, compared to the device with 90° taper angle but without black matrices, while keeping unnoticeable color shift.
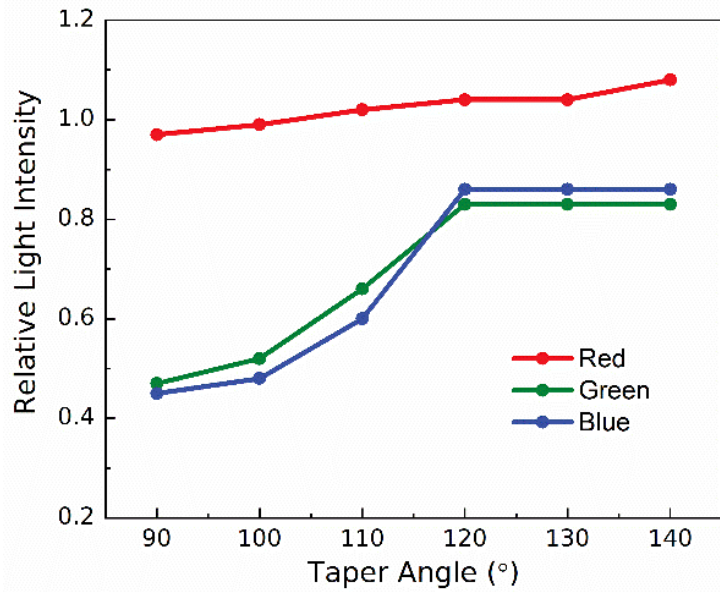
Figure 2-11 Relative light intensity as taper angle α changes.

The simulated color shifts for RGB micro-LED display with top black matrix and 120° taper angle is plotted in Fig. 2-12. The average $\Delta u'v'$ of all 10 reference colors at 80° is 0.005 and the maximum value is 0.014 for magenta channel, which is below 0.02 and is acceptable for commercial applications.
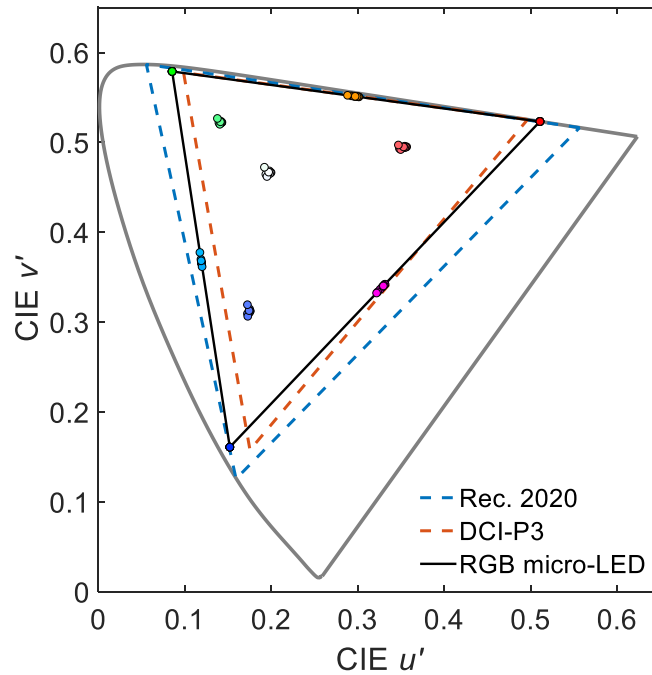
Figure 2-12 Simulated color shifts of 10 reference colors from 0° to 80° viewing angle for RGB micro-LED display with top black matrix and 120° taper angle.

Besides these 10 reference colors, we also evaluate the color shift using the first 18 colors in Macbeth ColorChecker [73], which is commonly used in color tests and reproductions to mimic the colors of natural objects such as human skin, foliage and flowers. Figure 2-13 depicts the simulated results. The color shifts of all 18 reference colors within 80° viewing cone are below 0.01 and the maximum average $\Delta u'v'$ is 0.007, which remains visually unnoticeable by human eye.
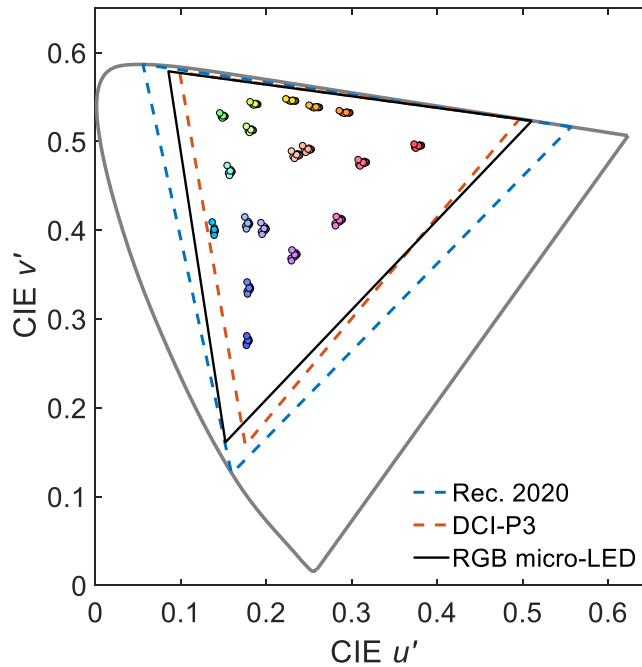
Figure 2-13 Simulated color shifts of the first 18 colors in Macbeth ColorChecker from 0° to 80° viewing angle for RGB micro-LED display with top black matrix and 120° taper angle.

In the above analysis, we discuss the color shift of RGB micro-LED displays when the viewing angle θ (polar angle) changes along a fixed azimuthal angle φ. It is noteworthy that the sidewall emission from a bare LED without black matrix will not stay the same when the azimuthal angle changes because it has a rectangular shape. As a result, the angular distributions would be different, leading to different levels of color shifts of RGB micro-LED display as the azimuthal angle changes. With the presence of black matrix, the color shift can be greatly suppressed at all polar angles and azimuthal angles because all the sidewall emissions are effectively absorbed and matched angular distributions for both RGB colors can be obtained, as shown in Fig. 2-14. In addition, the black matrices help to absorb the ambient light reflected from the micro-LED chips and metal wires, which in turn improves the ambient contrast ratio [10,74]. Other approaches to reduce color shift include making asymmetric subpixel arrangement [75] or employing a patterned

23

scattering film on top of the display panel to achieve matched angular distributions [76]. Each approach has its own merits and demerits.
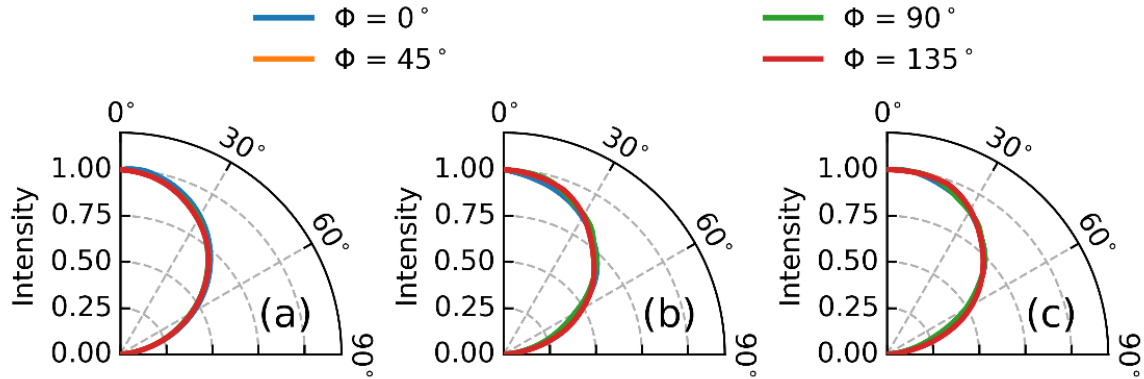
Figure 2-14 Simulated radiation patterns of (a) red, (b) green, and (c) blue micro-LEDs with top black matrix and 120° taper angle at different viewing angle θ and azimuthal angle φ.

<div align="center">2.5 Discussions</div>

As discussed in above sections, the angular color shift of RGB micro-LED display originates from angular distribution mismatch. To better understand their relationship, we investigate the maximum tolerable angular distribution mismatch while keeping indistinguishable color shift within the ±85° viewing zone. At normal viewing angle, the RGB ratio [a, b, c] to obtain a white point D65 can be calculated using the following equation [68]:

$$
\begin{bmatrix} X_R & X_G & X_B \\ Y_R & Y_G & Y_B \\ Z_R & Z_G & Z_B \end{bmatrix} \begin{bmatrix} a \\ b \\ c \end{bmatrix} = \begin{bmatrix} X_t \\ Y_t \\ Z_t \end{bmatrix},
\tag{5}
$$

In Eq. (5), X, Y, Z are tristimulus values for colored stimuli and can be obtained by multiplying the color matching functions $\bar{x}(\lambda)$, $\bar{y}(\lambda)$ and $\bar{z}(\lambda)$ by the amount of energy I(θ) in the stimulus at each wavelength and integrating across the spectrum S(λ) as shown in Eq. (6) [68].

$$X = \int I(\theta)S(\lambda)\bar{x}(\lambda)d\lambda,$$
$$Y = \int I(\theta)S(\lambda)\bar{y}(\lambda)d\lambda, \qquad (6)$$
$$Z = \int I(\theta)S(\lambda)\bar{z}(\lambda)d\lambda,$$

After obtaining RGB ratio [a, b, c] at normal viewing angle, we can use it to calculate the color difference $\Delta u'v'$ at oblique viewing angle. While in our analysis, we keep $\Delta u'v'$ of white point is 0.014 which is corresponding to 3.5 Just Noticeable Color Difference (JNCD), and then calculate the tolerable angular distribution mismatch among RGB emissions by using Eq. (7):

$$S(\theta, \lambda) = a \cdot I_R(\theta) \cdot S_R(\lambda) + b \cdot I_G(\theta) \cdot S_G(\lambda) + c \cdot I_B(\theta) \cdot S_B(\lambda). \qquad (7)$$

The calculated results are depicted in Fig. 2-15. Here we assume the blue and green chips have the same angular distributions, and red chips have *Lambertian* (Fig. 2-15(a)) or *Batwing* distribution (Fig. 2-15 (b)). From the results, we conclude that only if the angular distributions of blue and green micro-LEDs are within the marked blue region, the color shift of white point is below 0.014. In other words, the angular distribution of RGB chips are not necessary to be exactly the same. This tolerance provides a useful guidance for further optimizing the display structure in order to reduce color shift and improve light efficiency simultaneously. For instance, microstructures can be employed helps improve the light efficiency and modify the angular distribution.
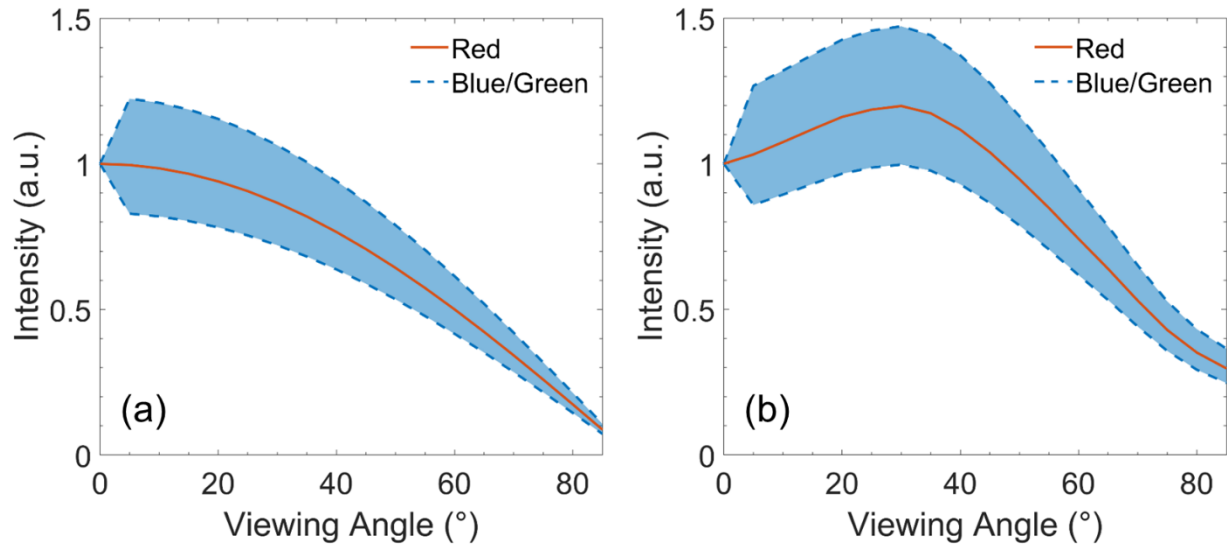
Figure 2-15 The tolerance of angular distribution difference of RGB micro-LEDs when the Δ*u′v′* of white point D65 is 3.5 JNCD. The radiation pattern of red micro-LED is (a) *Lambertian* **and (b)** *Batwing* **distribution, respectively.**

2.6 Microstructures for Improvement of Light Extraction Efficiency

Surface roughness and microstructures have been used to break the total internal reflection at the semiconductor-air interface and improve the light extraction efficiency of traditional LEDs [77,78]. They can be realized through different etching processes. In this dissertation, we investigate how the microstructures affect the light output when they are on micro-LED chip, on packing resin, and on both surfaces. Figure 2-16 illustrates three device structures with microsphere. For the microsphere on the resin, it can be fabricated as either hole or bump, which are referred to as microsphere-hole and microsphere-bump in this chapter. The reference micro-LED chip has a taper angle of 120° and reflector on the sidewall to improve the light output efficiency as discussed in Section 2.4.
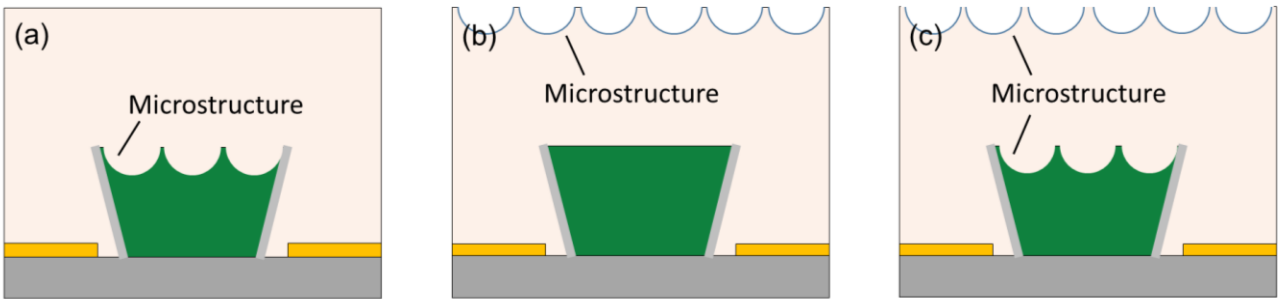
Figure 2-16 Schematic diagram of micro-LED with microsphere on (a) micro-LED chip, (b) packing resin, and (c) both chip and resin.

2.6.1 Microsphere on Micro-LED Chip
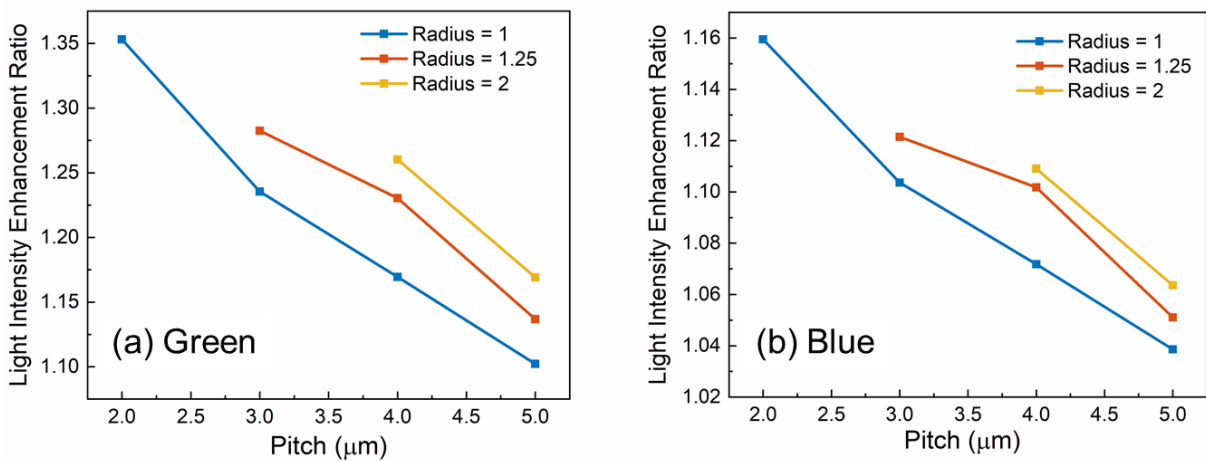
Figure 2-17 Light intensity enhancement ratio of microsphere-hole on (a) green and (b) blue micro-LEDs.

First, we investigate the effect of microsphere only on micro-LED chip by using ray tracing in LightTools. Light enhancement ratio to the structure without microsphere are calculated and results are plotted in Fig. 2-17. The radius and pitch of microsphere are chosen as variables. Considering the thickness of top n-GaN layer is only 2.5 μm in our chip, the radius of the microsphere changes from 1 to 2 μm. Besides, no microstructures are applied to the red micro-LED due to its thin epitaxial layer. As it can be seen, smaller pitch size and larger radius leads to

higher light enhancement ratio. For a certain pitch, the highest enhancement ratio can be obtained when the pitch to radius ratio equals to 2, which means the microsphere with larger density is preferred. Here, we select pitch = 2 μm and radius = 1 μm in the following simulation, and the corresponding light intensity enhancement ratio is 1.35 and 1.16 for the green chip and the blue chip, respectively.

2.6.2 Microsphere on Resin

Microsphere on micro-LED helps to extract light outside of chips, however, the total internal reflection also occurs at the resin-air interface, which reduces the overall light output efficiency. Therefore, in this section, we calculate the light enhancement ratio by optimizing the radius and pitch of microsphere-hole on the packing resin. Results for RGB micro-LED devices are depicted in Fig. 2-18. As pitch length increases, the light enhancement ratio first decreases sharply and then saturates at 1, indicating the number of microspheres is too small to help with light extraction. In addition, a larger radius is preferred to obtain higher light enhancement ratio. This trend is very similar to that microsphere on micro-LED discussed in the above section. Again, when the pitch to radius ratio equals to 2, highest light enhancement ratio can be achieved, which are 1.16 and 1.10 for green and blue chips, respectively. While for red micro-LED, the efficiency improvement is negligible because of the high refractive index ($n \approx 3.3$) of epitaxial material and large absorption loss of GaInP/AlGaInP MQWs. As a result, most of the emission is still trapped inside the red chip.
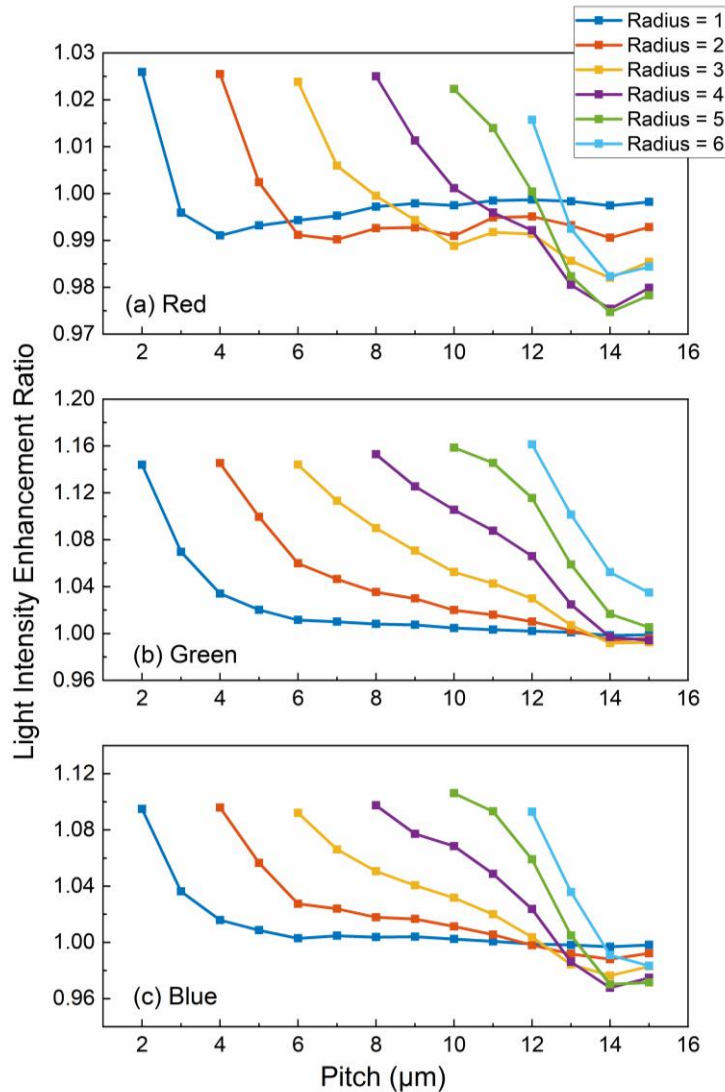
Figure 2-18 Light intensity Enhancement ratio of microsphere-hole on packing resin for (a) red, (b) green and (c) blue micro-LEDs.

In addition to microsphere-hole, we also study microsphere-bump on resin and results are plotted in Fig. 2-19. As expected, similar trend that smaller pitch length and lager radius enable higher light enhancement ratio is observed. Moreover, the ratio value is slightly higher compared to that with microsphere-hole. The reason is that microsphere-bump helps to converge the forward emission thus more light is collected by the receiver. However, besides light extraction efficiency

improvement, matched RGB angular distributions also need to be taken into consideration in order to keep an indistinguishable angular color shift, which will be discussed later.
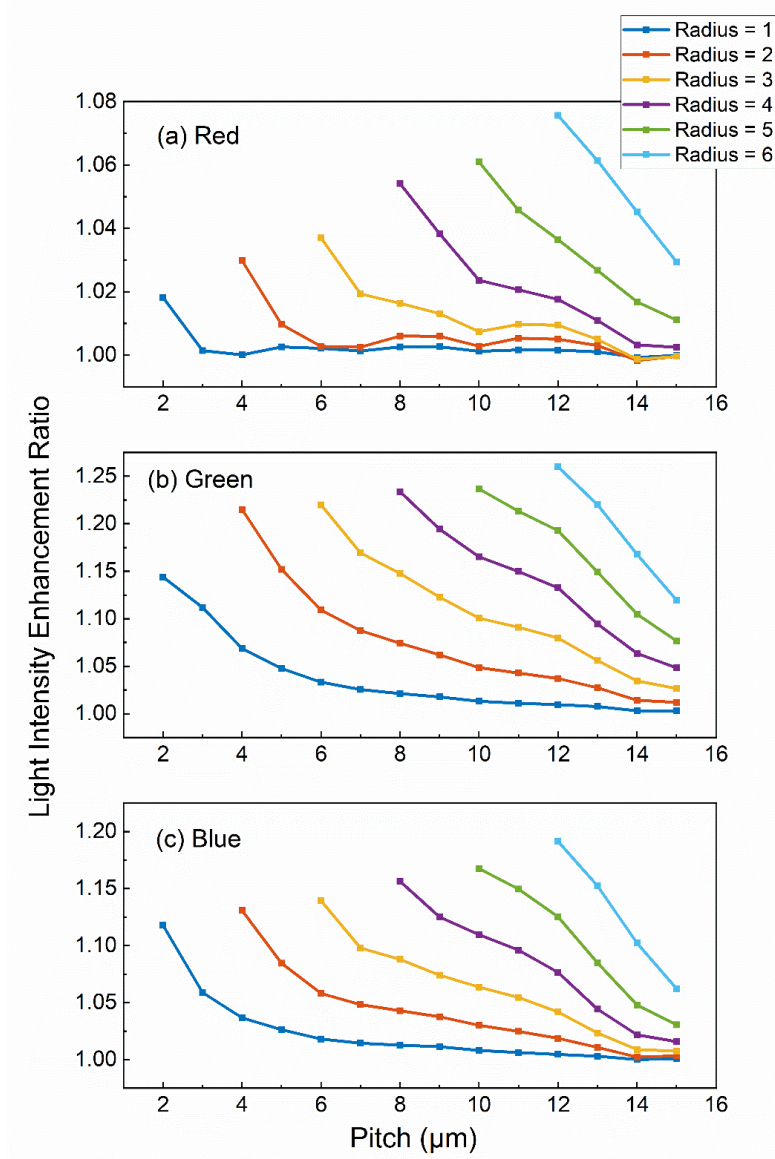
Figure 2-19 Light intensity Enhancement ratio of microsphere-bump on packing resin for (a) red, (b) green and (c) blue micro-LEDs.

2.6.3 Microsphere on Micro-LED and Resin

Figure 2-20 compares the raytracing results in structure without microsphere, microsphere on chip, on resin and on both chip and resin. The preview ray number is 100. When no microsphere is on micro-LED (Fig. 2-10(a) and (c)), it can be observed that the light is trapped inside the chip due to the total internal reflection at the LED-resin interface. For comparison, in Fig. 2-10(b) and (d), more light is extracted into the resin with the help of microsphere. With microsphere on resin, the light extraction efficiency is further improved.
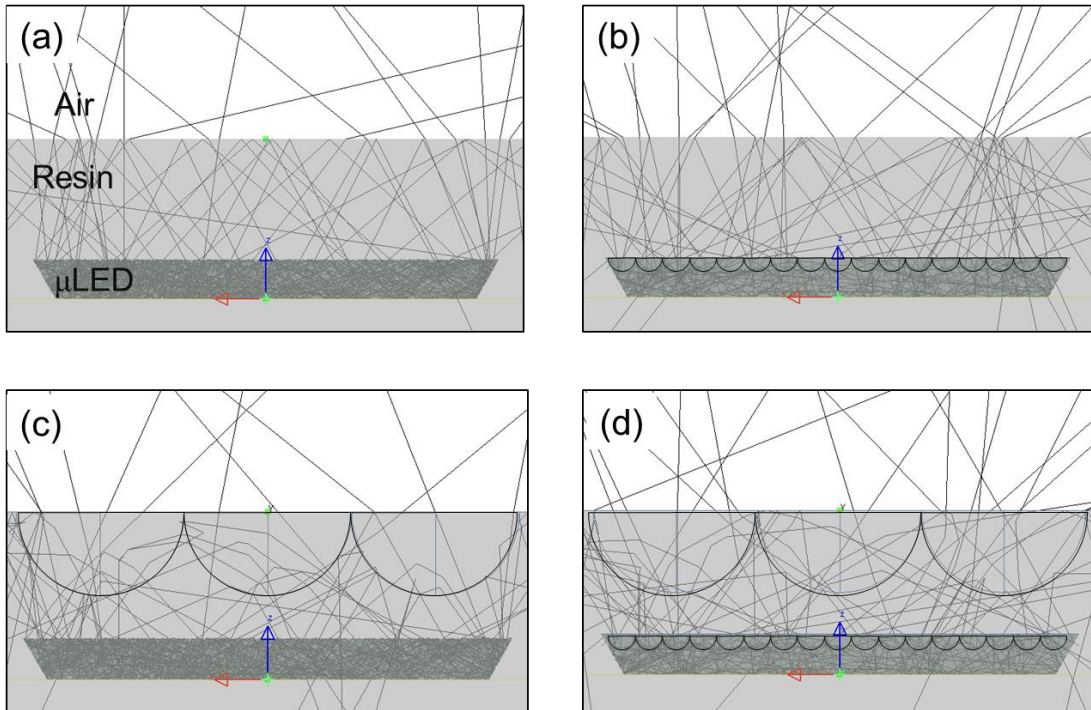
Figure 2-20 Ray tracing in micro-LEDs: (a) without microsphere, microsphere-hole on (b) chip, (c) resin and (d) both chip and resin.

Table 2-3 lists the light enhancement ratio of different devices. The pitch = 2 μm and radius = 1 μm for microsphere on micro-LED, and pitch = 12 μm and radius = 6 μm for that on resin. For structures D and E with microsphere on both chip and resin, the light output efficiency for green

and blue is improved by more than 50% and 35% compared to the structure without microsphere, which is promising for saving the power consumption of micro-LED displays.

Table 2-3 Light enhancement ratio of RGB micro-LEDs with microsphere.

Structure	Red	Green	Blue
A: Hole on LED	1.00	1.35	1.16
B: Hole on resin	1.01	1.16	1.10
C: Bump on resin	1.08	1.26	1.18
D: Hole on LED + Hole on resin	1.02	1.54	1.35
E: Hole on LED + Bump on resin	1.07	1.69	1.50
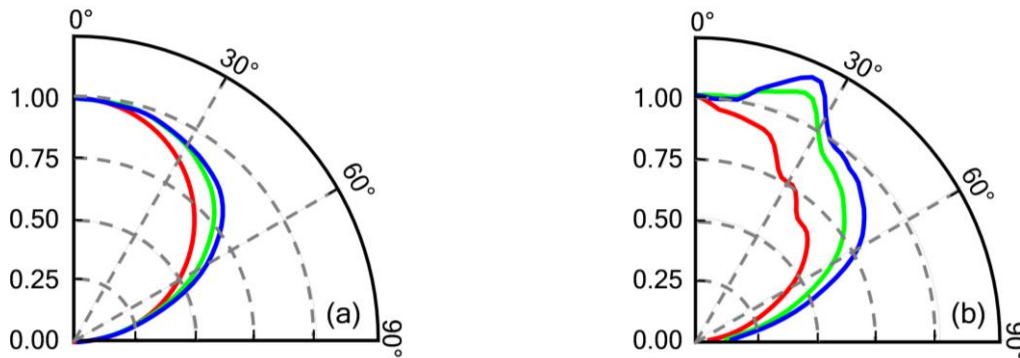
Figure 2-21 Simulated radiation patterns of (a) structure D with microsphere-hole and (b) structure E with microsphere-bump. RGB lines represent RGB micro-LED, respectively.

For structures D and E, we calculate the radiation patterns of RGB device and results are shown in Fig. 2-21. It can be observed that although structure D has a lower light enhancement ratio, its RGB angular distributions are more matched than those of structure E, which enable a lower color shift at large viewing angle. Figure 2-22 depicts the simulated color shift of structure

D from 0° to 80° viewing angle using the first 18 colors in Macbeth ColorChecker. The average color shifts of all reference colors within 80° viewing cone are 0.007, which is visually unnoticeable by human eye.
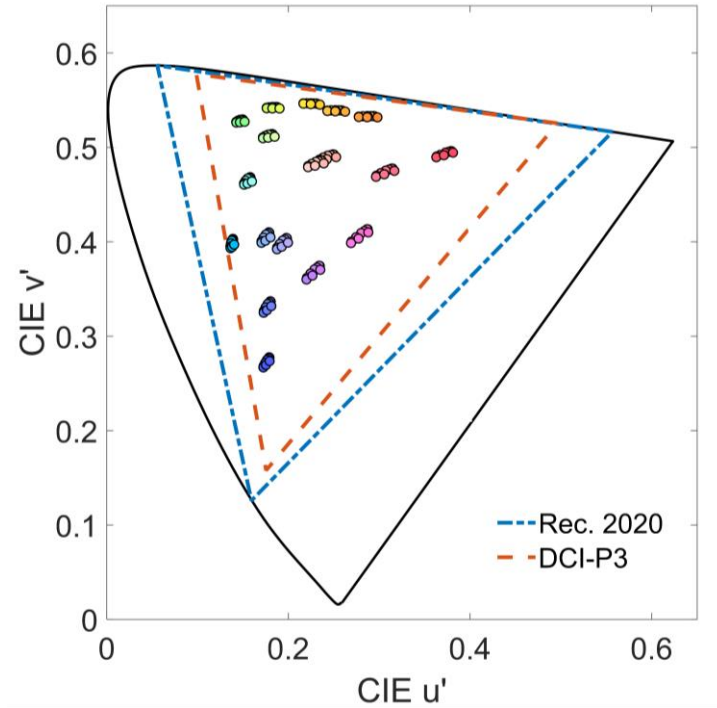
Figure 2-22 Simulated color shifts of the first 18 colors in Macbeth ColorChecker from 0° to 80° viewing angle for RGB micro-LED with microsphere-hole on both chip and resin.

2.7 Summary

In this chapter, we built an experiment-valid simulation model to analyze the color shift of RGB micro-LED displays. Results show that the sidewall emission causes mismatched angular distributions between AlGaInP-based red micro-LED and InGaN-based blue/green counterparts due to material difference, which further leads to visually noticeable color shift at larger viewing angle. To mitigate the color shift while keeping a high light extraction efficiency, a device structure with top black matrix and taper angle in micro-LEDs was proposed. After optimization, the color

shift $\Delta u'v'$ of the RGB micro-LED display with 120° taper angle is suppressed to below 0.01 within 80° viewing cone for the first 18 reference colors in Macbeth ColorCheker, and the efficiency keeps ~85% of the device without black matrix. To further improve the efficiency, we proposed microspheres with optimized size on both micro-LED chip and packing resin. For the green and blue devices, their light extraction efficiency is enhanced by 54% and 35%, respectively. Although only microsphere is discussed in this chapter, microstructure with other shape such as cones or pyramid can also be applied.

CHAPTER 3 : WHITE MICRO-LED

3.1 Background

To achieve full color micro-LED display while avoiding the challenging mass-transfer fabrication process, one approach is to utilize single color micro-LEDs to excite color converters, such as phosphors or quantum dots (QDs). For example, UV LED array with pixelated RGB quantum dots can achieve high efficiency and wide color gamut because no color filter is needed. However, to achieve complete color down-conversion, QDs with a high optical density and a relatively thick layer are required. Therefore, light recycling components such as distributed Bragg reflector are usually employed to improve the light conversion efficiency, which would degrade the ambient contrast ratio [79]. To overcome this problem, another approach is to employ blue micro-LEDs to excite color converters in order to obtain white light first, and then utilize color filters to achieve RGB subpixels [44], which is referred to as white micro-LEDs in this dissertation. In this device configuration, the color down-conversion layer does not need to be pixelated, which is more favorable from device fabrication viewpoint. However, the color filters would absorb 2/3 of the outgoing light. In addition, color crosstalk would occur due to scattering of the color conversion layer.

In this chapter, we propose a funnel-tube array for two-color phosphor based micro-LED displays to reduce color crosstalk and improve light conversion efficiency simultaneously. In addition, the issue of ambient light reflection from the device is addressed.
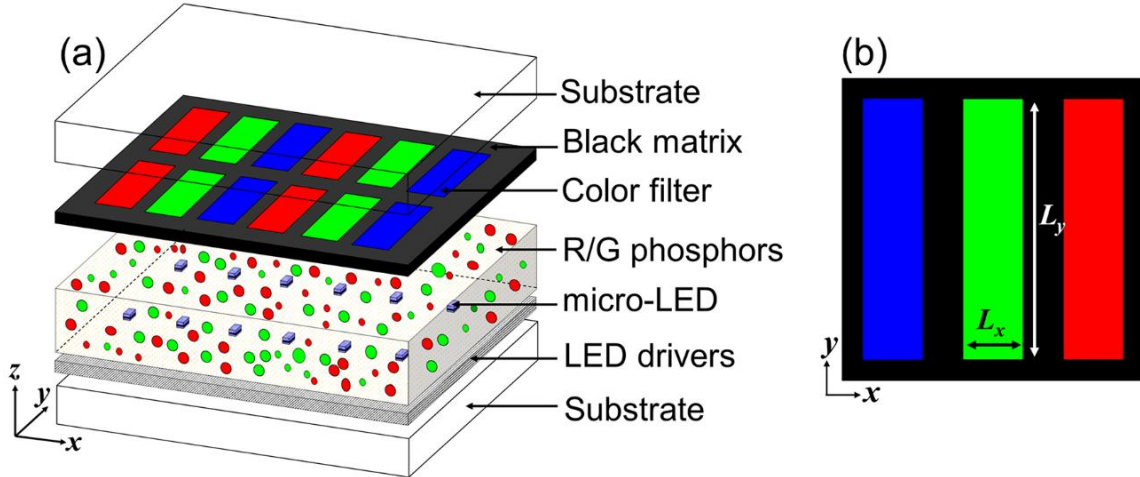
Figure 3-1 (a) Schematic diagram for configuration of full color micro-LED display (Device I). (b) Top view of one pixel. $L_x = 30$ μm, $L_y = 130$ μm.

Figure 3-1(a) illustrates the device structure of color-converted micro-LED displays (Device I). An array of monochromatic blue micro-LEDs with a LED driving backplane are formed on the bottom substrate. Above the micro-LED array, a layer of green and red phosphor is coated to obtain a white light source. On top of the phosphor, a color filter array is used to form RGB subpixels. The pitch length of the display panel is set to be 150 μm, and the color filter size is $L_x = 30$ μm and $L_y = 130$ μm (Fig. 3-1(b)). The chip size of blue micro-LED is $W_x = 15$ μm and $W_y = 30$ μm. The system is simulated using ray-tracing software LightTools. For simplicity, we assumed that all the micro-LEDs having the same central wavelength of 448 nm with *Lambertian* angular emission distribution. The phosphor photoluminescence is simulated using LightTools Advanced Physics Module [80]. The absorption spectrum, color conversion efficiency, and emission spectrum are all taken into account during calculations [81]. The phosphor particle size in the simulation is set to vary from 0.25 μm to 5 μm due to the small pixel size [82]. The refractive index of phosphor is 1.8 at all wavelengths. The concentrations of green and red phosphors are

adjusted to obtain a white point for the display system. Simulation process starts with the emission of blue light from the micro-LED array. When the light encountering phosphor particles, the blue light is partially absorbed or scattered by the phosphor particles. The absorbed blue light will be down-converted to green and red light with isotropic radiation, while the scattered light has intensity distributions calculated by Mie theory [83]. Re-absorption of green and red light by the phosphor particles is also considered in the modeling. Compare to QDs, phosphors have the advantages of over 80% quantum yield, high thermal stability, resistance to moisture and stable quantum yield and spectral properties [84].

In Device I, when only one pixel emits light and all other pixels are turned off, light leakage may come from the surrounding pixels due to light scattering of the phosphor film, which is referred to as color crosstalk. Figure 3-2 shows the simulated color image. Although only the RGB subpixels inside the white dashed lines are turned on, light leakage outside this region is clearly observed. This problem becomes more severe as the thickness of the phosphor film (h) increases [85].
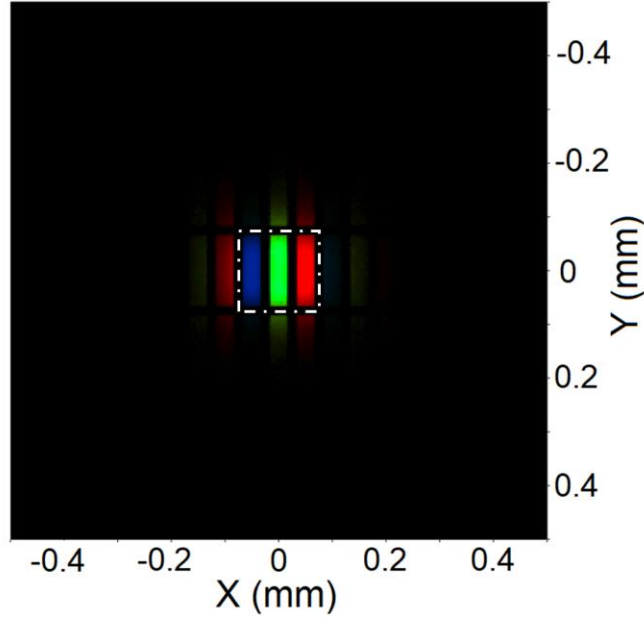
Figure 3-2 Simulated color image of Device I when only one pixel inside the white dashed lines is turned on.

To evaluate the color crosstalk quantitatively, we define the color crosstalk ratio as $R_{\text{crosstalk}}$, which can be calculated using Eq. (8):

$$R_{crosstalk} = \frac{I_{total} - I_{pixel}}{I_{total}}, \qquad (8)$$

where I_{total} represents the total intensity of the whole panel ($\gg 10$ pixels), and I_{pixel} stands for the light intensity from the turned-on pixel. Figure 3-3 plots the calculated color crosstalk as a function of the phosphor thickness h in Device I. When h increases from 15 μm to 100 μm, the optical path inside the phosphor film becomes longer, leading to a more severe light scattering. Therefore, the color crosstalk of RGB subpixels increases accordingly.
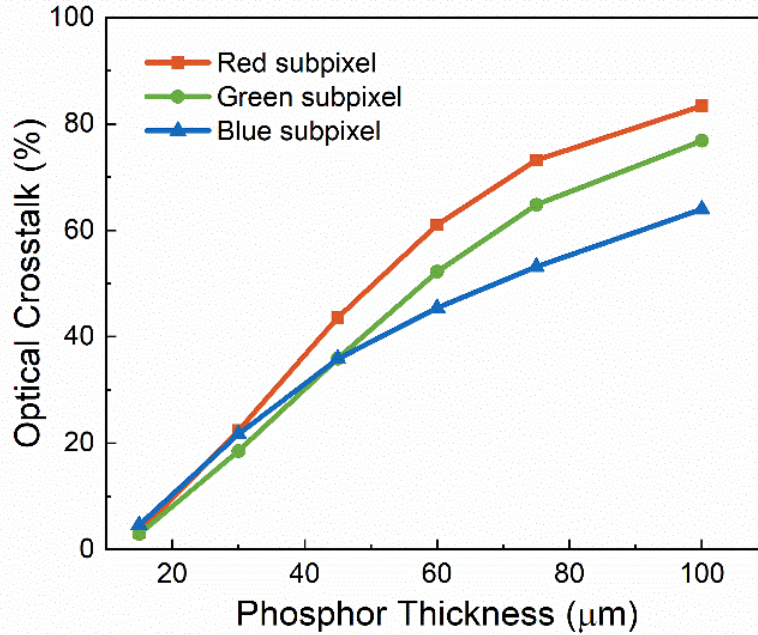
Figure 3-3 Simulated color crosstalk of Device I as a function of phosphor thickness.

To eliminate color crosstalk, we propose Device II with funnel-tube array and taper angles α (*x-z* plane) and β (*y-z* plane) as illustrated in Fig. 3-4. It is formed above micro-LED layer while the tube region aligned with each subpixel. The inner surface of the funnel-tube can be either absorptive or reflective. The two-color phosphors are filled inside the funnel-tube to obtain white light. On top of the funnel-tube array, the color filters with RGB subpixels are aligned with each tube region. The simulation parameter is set to be the same as in Device I: $W_x = 15$ μm, $W_y = 30$ μm, $L_x = 30$ μm and $L_y = 130$ μm. In the system, the phosphors for each subpixel region are designed to be totally isolated. Thus, the color crosstalk will be eliminated. Figure 3-5 shows the simulated color image of Device II. As it can be seen, there is no light leakage outside the turned-on pixel region.
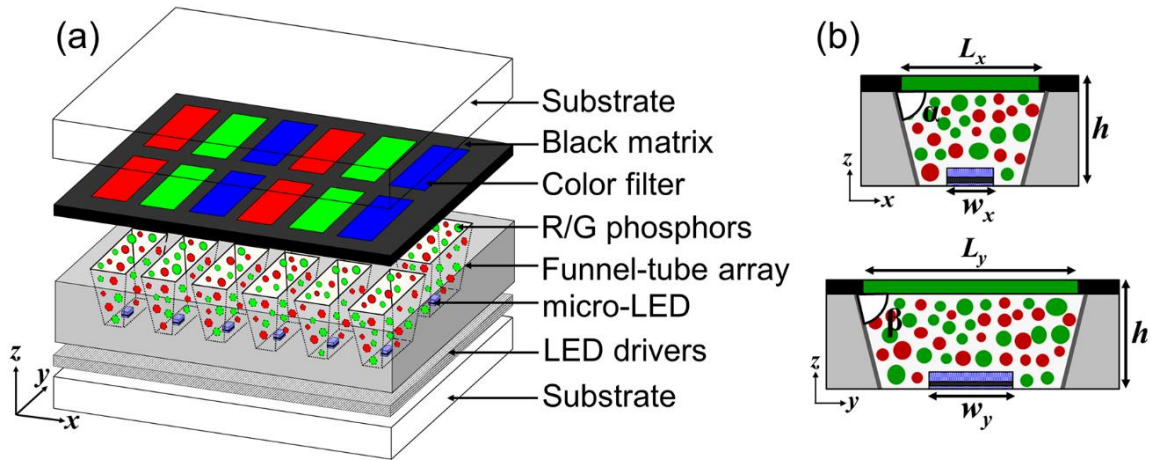
Figure 3-4 (a) Schematic diagram for configuration of full color micro-LED display with funnel-tube array (Device II). (b) Cross-sectional views of Device II. The taper angles in *x-z* plane and *y-z* plane are α and β, respectively.
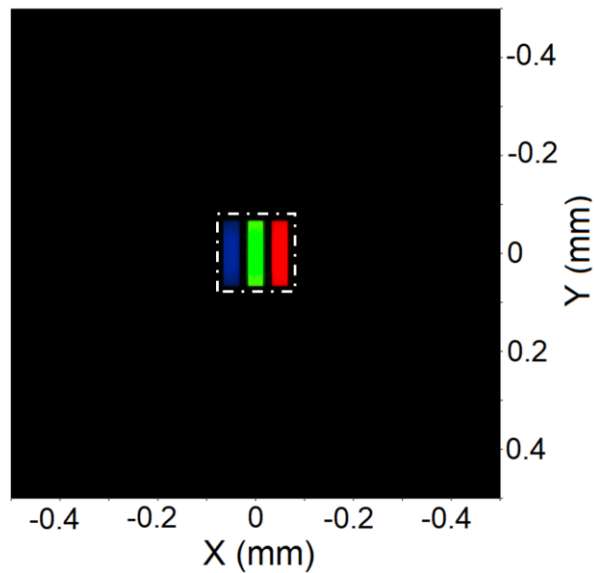
Figure 3-5 Simulated color image of device II when only one pixel which inside the white dashed line is turned on.

3.3 Color Gamut

Vivid color is a key metric for display devices, as it enables a more realistic viewing experience. Generally, light sources with a narrower full width at half maximum (FWHM) would

lead to a wider color gamut [56]. In our modeling, we use a combination of green phosphor (β-sialon:Eu2+, FWHM ~ 50 nm) and red phosphor ($CaAlSiN_3:Eu^{2+}$) [86] to improve the color performance. Figure 3-6 depicts the spectrum of blue micro-LED pumped the two-color phosphors and the simulated color gamut in CIE 1931 color space is shown in Fig. 3-7. This system covers 92% of DCI-P3 standard [87] and 67% of Rec. 2020 standard [88,89]. Alternative color converters such as CdSe red/green QDs with FWHM ~ 25–30 nm can also be used to obtain wider color gamut [19,57]. However, the device structure, especially the thickness of the funnel-tube array, needs to be optimized according to the optical density of the color converters.
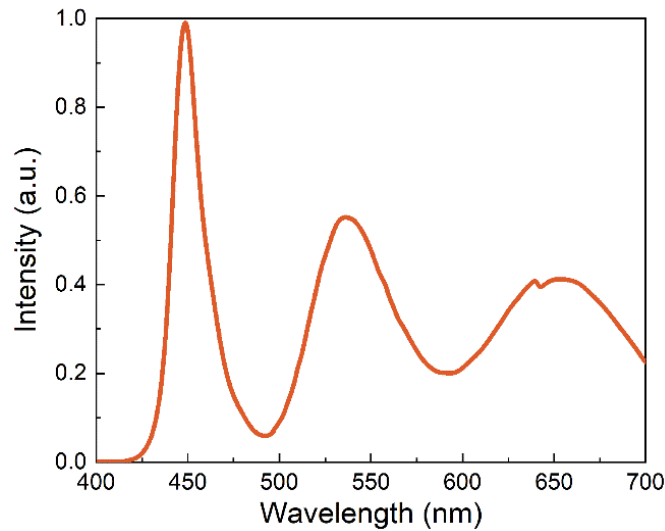
Figure 3-6 Simulated spectrum of device II when all of the pixels are turned on.
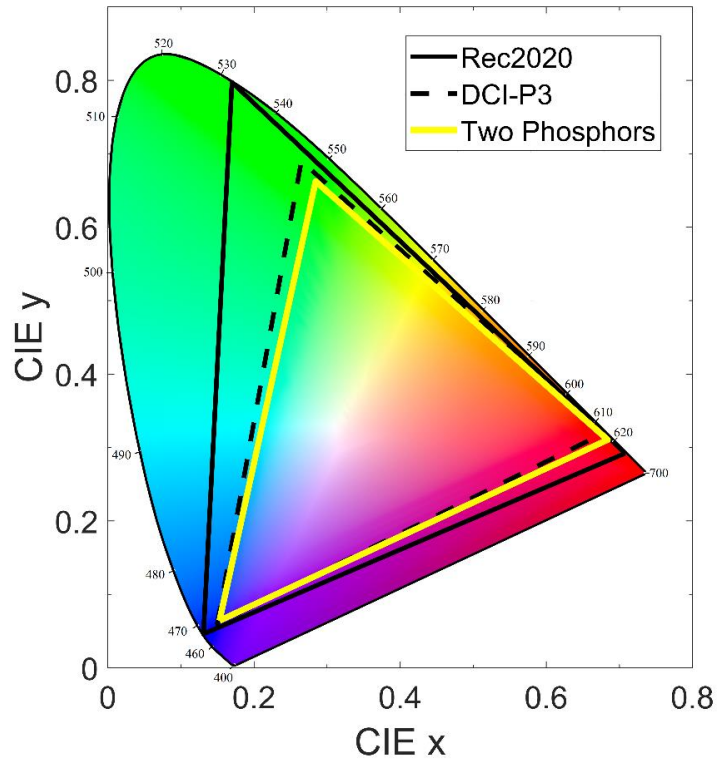
Figure 3-7 Simulated color gamut for Device II with red/green phosphor in CIE 1931 color space.

<u>3.4 Light Efficiency and Ambient Contrast Ratio</u>

3.4.1 Reflective Coating

In addition to color crosstalk, power consumption is another critical performance metric for displays. To improve the light efficiency, the inner surface of funnel-tube can be deposited metallic reflectors to recycle light and elongate the effective optical path inside the phosphors. Furthermore, the taper angles (α and β) of the funnel-tube need to be optimized. The simulated relative light intensities of Device II with reflective coatings normalized to that of Device I are plotted in Fig. 8. Specifically, in Fig. 3-8(a), the taper angle α varied from 76° to 108°, while β was fixed at 80°; in Fig. 3-8(b), the taper angle β varied from 31° to 108° when α was set to be

80°. As can be seen from these figures, the light intensity decreases as the taper angle increases. When taper angle is larger than 90°, more light will be reflected downwards by the inner reflector and then absorbed or scattered by the backplane. On the other hand, when taper angle is less than 90°, more light could be reflected upwards and then escape from the device to the air. Therefore, taper angle less than 90° is preferred to obtain higher light efficiency. However, the ambient light reflectance also increased as illustrated in Fig. 3-8 (right scale), which would degrade the ambient contrast ratio of the displays.
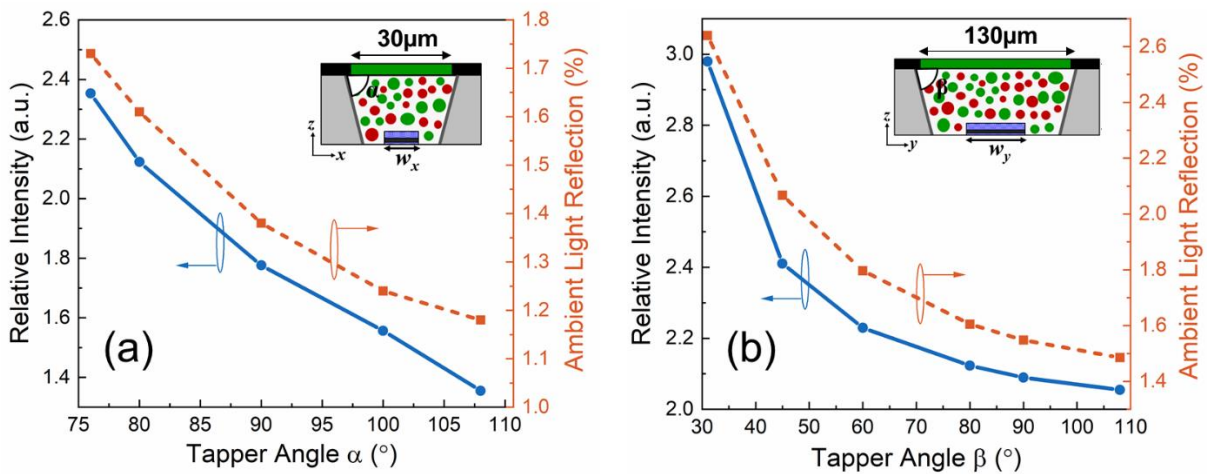
Figure 3-8 Relative light intensity of Device II with reflective coating as a function of taper angle: (a) α when ß = 80°, and (b) ß when α = 80°. The light intensity is normalized to that of device I.

In order to further understand the ambient light reflection, we plot the reflectance for RGB subpixels of structure with reflective coating and α = 80° and β = 80° as well as transmittance of color filters in Fig. 3-9. The reflectance spectral profiles are very similar to the transmittance of color filters except for the lower intensity of the blue light. For the blue subpixel, the blue component of the ambient light transmitted through the color filter and entered the funnel-tube, some of the light was absorbed and then converted by the phosphor, and other light was scattered

and reflected inside the funnel tube. A part of the unconverted blue light could escape from the color filter. For green and red subpixels, the ambient light was scattered by the phosphor particles or reflected by the funnel-tube back to the air, leading to higher reflectance.
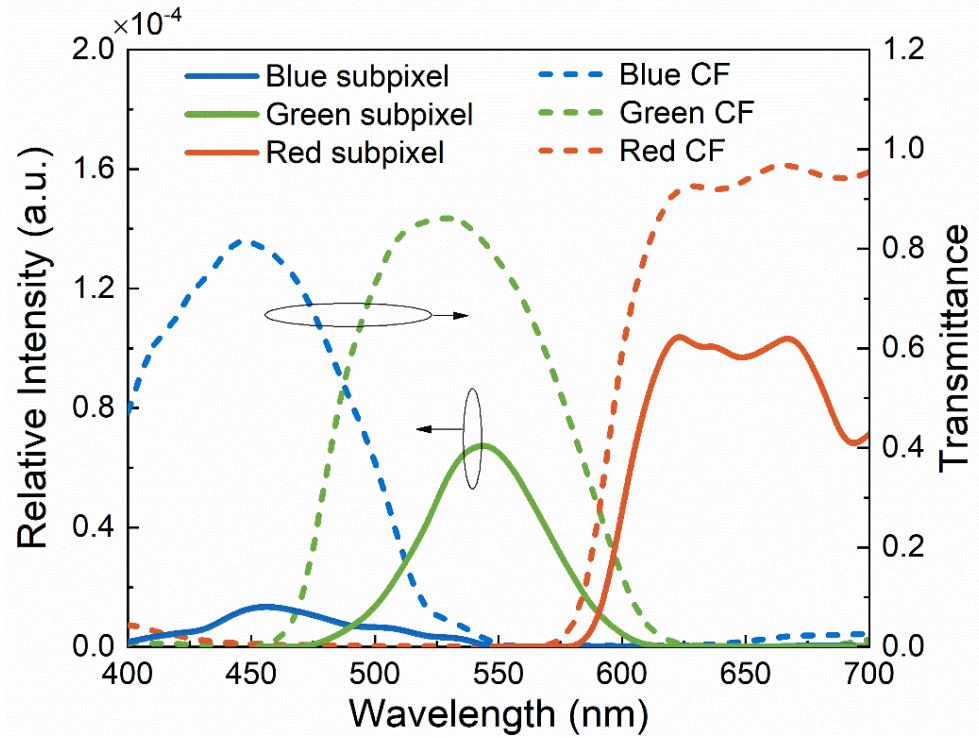
Figure 3-9 Ambient light reflectance (solid lines, left y axis) for RGB subpixels of Device II with reflective coating and taper angle α = 80° and ß = 80°, and transmittance of RGB color filters (dashed lines, right y-axis).

Luminous ambient light reflectance can be defined as [90]:

$$R_L = \frac{\int_{\lambda_1}^{\lambda_2} V(\lambda)S(\lambda)R(\lambda)d\lambda}{\int_{\lambda_1}^{\lambda_2} V(\lambda)S(\lambda)d\lambda}, \quad (9)$$

where $V(\lambda)$ is the photopic human eye sensitivity function, $R(\lambda)$ is the spectral reflectance of the display device, and $S(\lambda)$ is the spectrum of ambient light. In our modeling, we used CIE standard D65 as light source. Table 3-1 lists the luminous ambient light reflectance for each subpixel of

structure with reflective coating and α = 80° and β = 80°. Due to human eye sensitivity, ambient

reflection from green subpixel was dominant.

Table 3-1 Luminous ambient reflectance R_L for RGB subpixels of Device II with reflective coating and taper angle α = 80° and ß = 80°.

Pixels	RGB	Blue	Green	Red
R_L	1.61%	0.05%	1.02%	0.54%

To analyze how taper angle affects the optical performance, we chose three typical

structures: A (α= 108°, β = 108°), B (α = 90°, β = 90°) and C (α= 76°, β = 31°). The relative light

intensities $I_{emission}$ (which are normalized to the light intensity of Device I) and luminous ambient

reflectance of these three structures are listed in Table 3-2. Compared to Device I without funnel-

tube array, the light intensities of structure A, B and C are all improved, indicating higher optical

efficiency. Specifically, the light intensity of structure C is ~3X larger, but the luminous ambient

light reflectance also increases, which would degrade the ambient contrast ratio.

Table 3-2 Relative light intensity and luminous ambient reflectance of structure A, B and C with reflective coating.

Structure (α, β)	A (108°, 108°)	B (90°, 90°)	C (76°, 31°)
$I_{emission}$	1.20	1.60	2.93
R_L	1.12%	1.34%	2.64%

The ambient contrast ratio (ACR) of these three structures is calculated using following

equation [74,90]:

$$ACR = \frac{L_{on} + L_{ambient} \cdot R_L}{L_{off} + L_{ambient} \cdot R_L}. \qquad (10)$$

In Eq. (10), L_{on} (L_{off}) represents the on-state (off-state) luminance value of a display, $L_{ambient}$ is the ambient luminance and R_L is the luminous reflectance of the display panel.

To calculate ACR, we assumed L_{on} of Device I (without funnel-tube) to be 600 nits, while L_{on} of structures A, B and C can be calculated according to the relative intensity and the results are 720 nits, 906 nits and 1758 nits, respectively. For all structures, L_{off} is 0, the surface reflectance is assumed to be 4.5%. The calculated ACR of structures A, B and C are plotted in Fig. 3-10. As the ambient light gets stronger, the ACR decreases dramatically first and gradually saturates. Among these three structures, although structure C has the most severe ambient light reflectance, it achieves the largest ACR under different ambient light conditions due to its highest brightness. However, under strong ambient light conditions such as full daylight (~20,000 lux), the ACR of three structures are small ($\leqslant$ 5:1, inset of Fig. 3-10), which is barely readable under sunlight according to Table 3-3. This relatively low ACR originates from both light scattering by the phosphor particles and surface reflection. To improve ACR, commercial anti-reflection coating [91] with surface reflectance about 1.5% can be employed, and results are shown in Fig. 3-11. When $L_{ambient}$ = 20,000 lux, the ACR can be improved to above 5:1, which is adequately readable in sunlight [92].
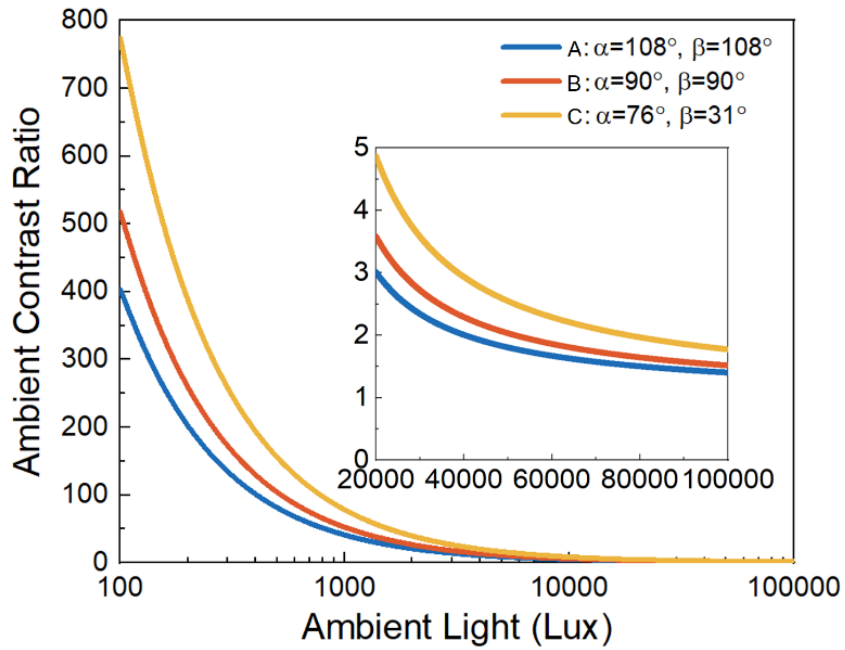
Figure 3-10 Simulated ambient contrast ratio of Ambient contrast ratio of structure A, B and C. The top surface reflectance is 4.5% without AR (anti-reflection) coating.
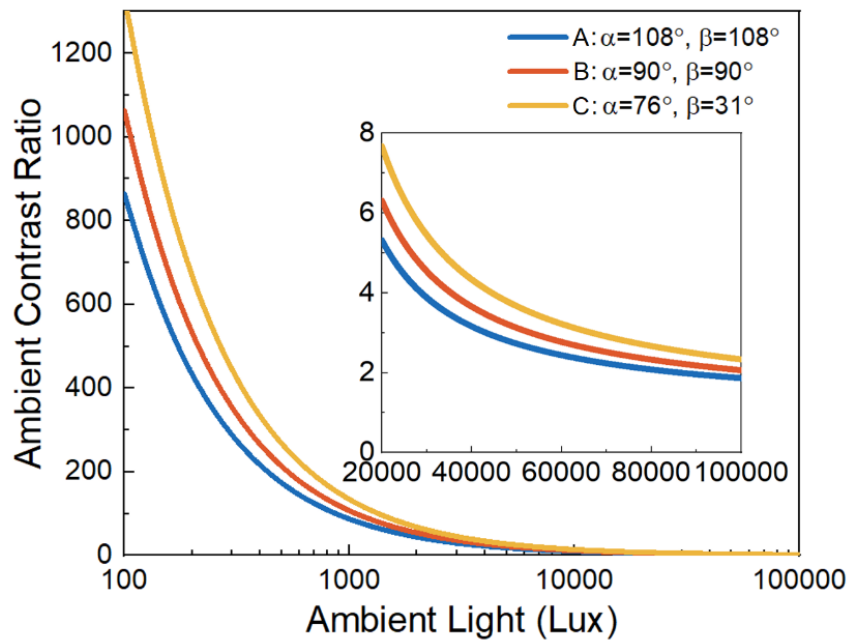
Figure 3-11 Simulated ambient contrast ratio of Ambient contrast ratio of structure A, B and C. The top surface reflectance is 1.5% with AR (anti-reflection) coating.

Table 3-3 ACR vs. sunlight readability [92]**.**

ACR	Sunlight readability
1-2	Unreadable in sunlight
3-4	Adequately readable in shade; barely readable in sunlight
5-9	Adequately readable in sunlight; looks OK
10	Very readable in sunlight; looks good
15	Outstanding readability; looks great
20	Totally awesome; excellent readability; can't be improved

3.4.2 Absorptive Coating

Another approach to reduce the ambient light reflection is to use absorptive material for the funnel-tube array, but the tradeoff will be reduced light efficiency. We calculate the relative light intensities of Device II with absorptive coatings normalized to that of Device I. Results are plotted in Fig. 3-12. Specifically, in Fig. 3-12(a), the taper angle α varied from 76° to 108°, while α was fixed at 80°; in Fig. 3-12(b), the taper angle β varied from 31° to 108° when α was set to be 80. Different from the results for the reflective coating as shown in Fig. 8, for absorptive coating the light intensity slightly increased as taper angle increased because more forward emission was absorbed. The relative intensity is only 0.62 even for α = 108° and β = 80°, which is >2X lower compared to the reflective coating structure. However, the ambient light reflectance becomes lower as expected, which may help to improve the ambient contrast ratio.
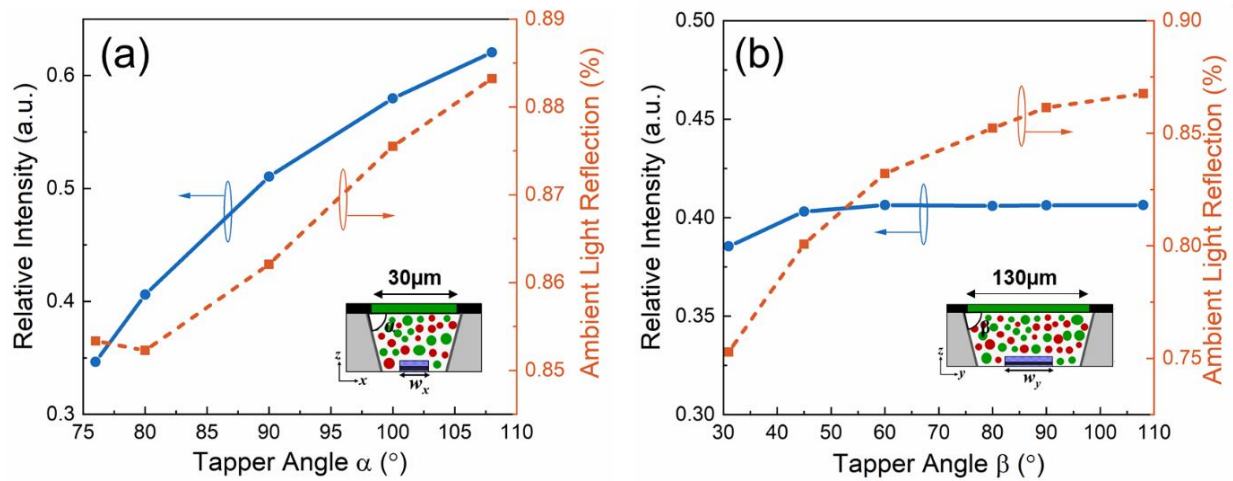
Figure 3-12 Relative light intensity of Device II with absorptive coating as a function of taper angle: (a) α when ß = 80°, and (b) ß when α = 80°. The light intensity is normalized to that of device I.

Table 3-4 lists the relative light intensity and luminous ambient reflectance of Device I without funnel tube and Device II with absorptive and reflective coatings. Although absorptive coating helps to reduce ambient reflectance by about 2X compare to reflective coating, the light intensity is sacrificed by more than 5X, which causes much larger power consumption.

Table 3-4 Relative light intensity and luminous ambient reflectance of Device I (without funnel tube) and Device II with absorptive and reflective coatings. The taper angle α = 80° and β = 80°.

Device	W/O funnel tube	Absorptive coating	Reflective coating
$I_{emission}$	1.00	0.41	2.12
R_L	0.96%	0.85%	1.61%

To compare the ACR of different coatings, we choose Device II with absorptive and reflective coatings with taper angle α = 80° and β = 80°. Their L_{on} are calculated to be 246 nits and

1272 nits according to the relative intensity to Device I (without funnel-tube) with L_{on} = 600 nits.

The surface reflectance was assumed to be 4%. Figure 3-13 plotted the calculated ACR. Although funnel-tube with reflective coating had the most severe ambient reflection, it achieved the largest ACR under different ambient light conditions due to its highest brightness. Under strong ambient light conditions such as full daylight (~20,000 lux), the ACR of Device I and Device II with absorptive coating were all < 5:1 (inset of Fig. 3-13), which is barely readable under sunlight. To improve ACR, we also employed AR coating with a surface reflectance of 1.5% and results are shown in Fig. 3-14. When $L_{ambient}$ = 20,000 lux, the ACR of Device II with reflective coating could be improved to ~8:1, which is adequately readable in sunlight. While for Device II with absorptive coating, the improvement of ACR is minor and the readability still keeps poor. Therefore, reflective coating is preferred for the funnel-tube to improve the light efficiency while keep a good sunlight readability.
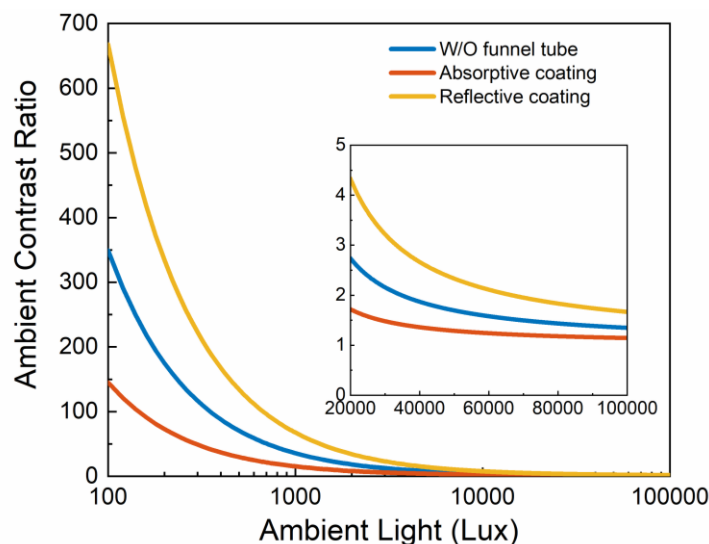
Figure 3-13 Simulated ambient contrast ratio of Device I and Device II with absorptive coating and reflective coating on the side inner surface of funnel-tube. Taper angle α = 80° and β = 80°. The top surface reflectance is 4.5% without AR coating.
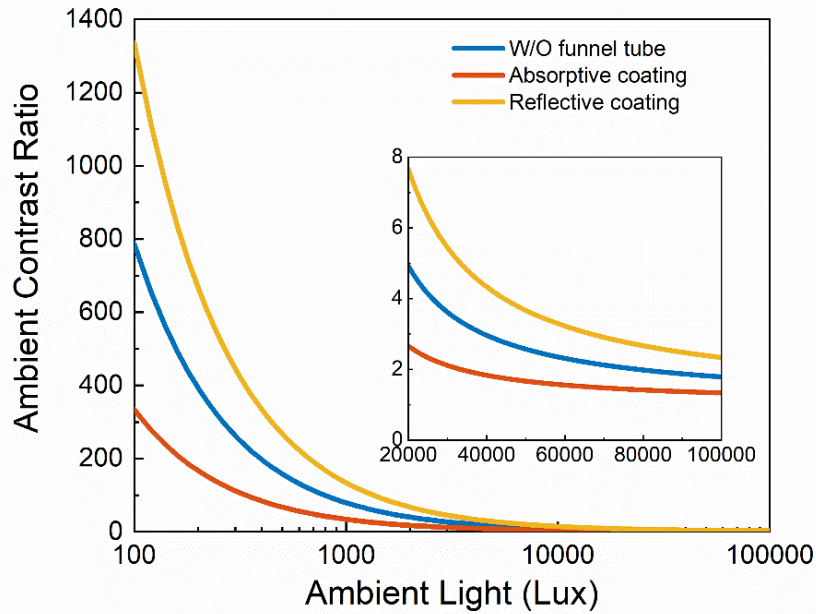
Figure 3-14 Simulated ambient contrast ratio of Device I and Device II with absorptive coating and reflective coating on the side inner surface of funnel-tube. Taper angle α = 80° and β = 80°. The top surface reflectance is 1.5% with AR coating.

3.5 Summary

In this chapter, we proposed a funnel-tube array to eliminate the color crosstalk of a two-color phosphor-converted white micro-LED displays. By depositing reflective or absorptive coating on the inner surface of the funnel-tube, a clear boundary was formed between the subpixels to prevent light leakage, thus a near zero optical crosstalk was achieved.

To improve the light output efficiency, the taper angle of the funnel-tube was also optimized. With reflective coating on the inner surface, the light efficiency of the device was enhanced by ~3X as the taper angle [α, β] equals to [76°, 31°]. Compare with the absorptive coating, the ambient contrast ratio with reflective coating is also improved due to higher light intensity despite the increased ambient reflectance. In addition, by utilizing two-color phosphors, which

51

have high thermal stability and resistance to moisture, the color gamut of this device covers 92%

of DCI-P3 standard.

CHAPTER 4 : QUANTUM DOT-CONVERTED MICRO-LED

4.1 Background

In recent years, quantum dots (QDs) have been widely used as color conversion layers in LCD backlight system due to their large absorption cross-section and narrow emission spectra (20~40 nm), which help to create vivid color image on displays [55,93–95]. These nanometer-sized (2~10 nm) semiconductor particles consist of core-shell structure and organic ligands and are mainly governed by the quantum confinement effects [96]. The emission spectrum of QDs can be tuned by varying their particle size with the same material system. This property enables a design freedom for display applications to achieve wider color gamut. Compared to typical phosphors, QDs with nanometer scale also have potential to improve luminance uniformity due to reduced light scattering. In addition to LCD backlight, QDs have also been used as color down-converters for monochromatic micro-LED display to achieve full color [18,97]. By employing monolithically fabricated blue or UV micro-LED array to pump QD material, we can avoid the challenging mass transfer process and only need one type of LED epitaxy wafer. Besides, this approach has potential to achieve high resolution density, especially for small-size display applications such as micro-displays or digital watches.

Different from application in LCD backlight in which QD layer is underneath a stack of optical films, for QD-converted micro-LED display, the QD materials are on the top surface. As a result, the QDs can not only be excited by light from micro-LED, but also the short-wavelength component of ambient light, which will degrade the ambient contrast ratio of displays. In order to solve this issue, it is necessary to explore how to analyze the ambient light excitation of QDs

quantitatively at first. However, until now, there is no detailed discussion on ambient contrast ratio evaluation of QD-converted micro-LED displays.

4.2 Theory and Modeling

Figure 4-1 illustrates the device structure of blue micro-LED array with red and green QD conversion layer. When the ambient light illuminates on the device, the ambient contrast ratio may degrade due to the QD excitation. For simplicity, we divide the ambient excitation of QDs into following three parts. 1) The first-time excitation. When the ambient light first hits the QDs, some of the incident light is absorbed and converted according to the QD's absorption and emission spectra, and then emits back to air. 2) The second-time excitation. This part refers to the unabsorbed ambient light when first passing through the QDs but is absorbed and converted after being reflected by the bottom micro-LEDs and traversing through the QD at the second time. 3) Reflection. This is the reflected ambient light by the micro-LED layer without being absorbed or converted by the QDs.
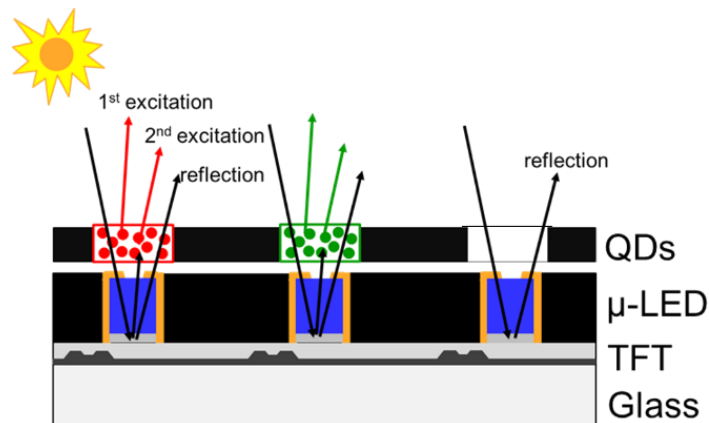
Figure 4-1 Device configuration of blue micro-LED array with red/green quantum dots as top color conversion layer.

54
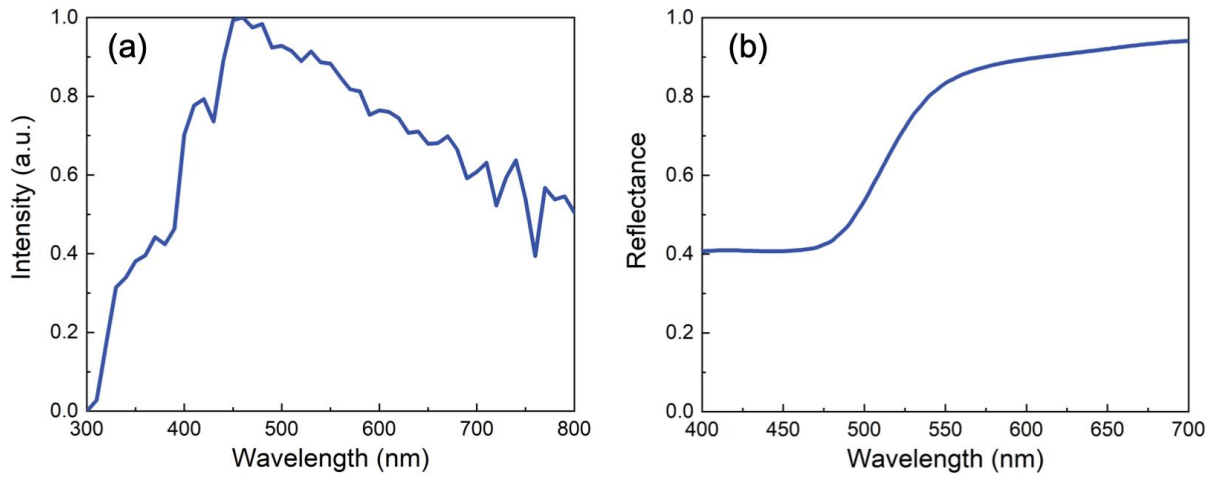
Figure 4-2 Simulation parameters. (a) Spectrum of D65 source. (b) Reflectance of micro-LED.
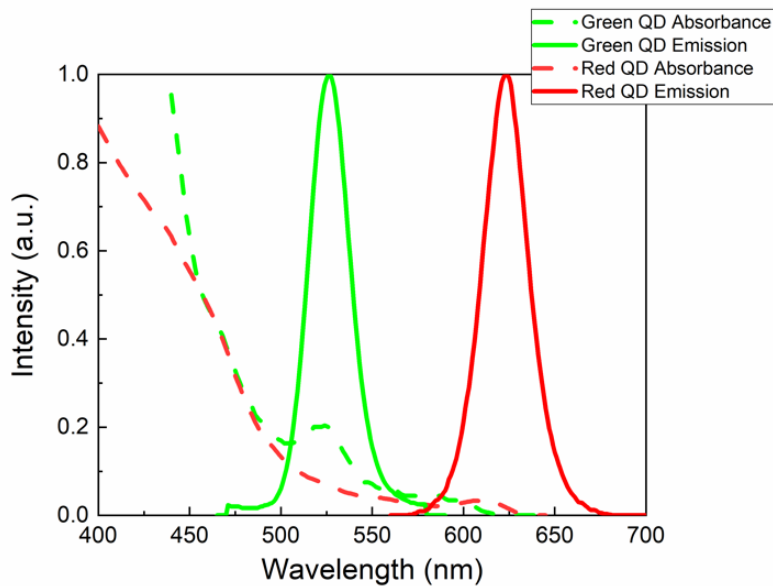
Figure 4-3 Absorbance and emission spectra of the employed green and red thick-shell quantum dots.

To quantitatively evaluate the ambient excitation of QDs, we use white light D65 as the ambient light source and its spectrum is plotted in Fig. 4-2(a). The reflectance of blue micro-LED is calculated with mixed-level simulation by combing Fresnel equation and ray tracing. For

simplicity, the micro-LED structure is assumed to be consisted of a 4-μm-thick GaN layer and a 100-nm-thick bottom gold electrode layer. The calculated reflectance is shown in Fig. 4-2(b). Fig. 4-3 shows the absorption and emission spectra of green and red QDs [98]. They are CdSe/CdS thick-shell QDs with low self-absorption and film photoluminescence quantum yield (PLQY) as high as ~70%. The absorbed number of photons (Nabs) by the QDs can be calculated by using Eqs. (11) and (12):

$$N_{abs}(\lambda) \cdot h\nu = I_{D65}(\lambda) \cdot A_{QD}(\lambda), \tag{11}$$

$$N_{abs} = \int I_{D65}(\lambda) \cdot A_{QD}(\lambda) \cdot \frac{\lambda}{hc} d\lambda, \tag{12}$$

where I_{D65} is the intensity of ambient light, A_{QD} is the absorbance of QDs, λ is the wavelength, h is the Planck constant, and c is the speed of light in vacuum. Then the emitted number of photons (N_{emit}) can be obtained according to the PLQY of the QD layer as:

$$N_{emit} = PLQY \cdot N_{abs}. \tag{13}$$

Therefore, the emitted light intensity from the QD layer can be calculated from following equation:

$$I_{emit} = I_{PL}(\lambda) \cdot \frac{PLQY \cdot \int I_{D65}(\lambda) \cdot A_{QD}(\lambda) \cdot \frac{\lambda}{hc} d\lambda}{\int I_{PL}(\lambda) \cdot \frac{\lambda}{hc} d\lambda}. \tag{14}$$

In Eq. (14), I_{PL} is the emission spectra of QD materials.

In order to verify above calculation model with MATLAB code, we also build a simulation model using commercial ray-tracing software LightTools [80]. Because the size of QD is in nanoscale, its photoluminescence (PL) is simulated using the mean free path, which is defined as

the average distance a ray travels inside the QD film before striking a QD nanoparticle [99,100]. The value of mean free path is adjusted to let all the blue light from micro-LEDs be absorbed. The absorption spectrum, PLQY (70%), and emission spectrum are all considered during simulations (Fig. 4-3). The refractive index of QDs is set to be 1.5 for all the wavelengths employed. Simulation process starts with the emission of ambient light source D65. When the light encountering QD particles, the ambient light is partially absorbed and converted to red or green light with isotropic radiation. While the unabsorbed light will continue to travel without changing its path [80].

4.3 Ambient Light Excitation of QDs

Figure 4-4 Calculated and simulated ambient light excitation spectra in quantum dot-converted micro-LED displays based on Matlab and LightTools.

Figure 4-4 depicts the calculated and simulated ambient light excitation spectra and they agree very well. These results show that the blue component of ambient light is nearly absorbed

and converted to red and green counterparts. Especially for the red component, the ambient excitation even exceeds 100%.

Figure 4-5 Calculated ambient light excitation and reflection for (a) red, (b) green and (c) blue subpixel in QD-converted full color micro-LED displays.

To further understand the ambient excitation of QDs, we plot the emitted light for RGB subpixels in Fig. 4-5. The area ratio of each subpixel to a whole pixel is assumed to be 1/3. For the red and green subpixels, the blue component of the ambient light is absorbed and converted by the QDs through first-time and second-time excitations, and other light is reflected by the bottom micro-LEDs. While for blue subpixel, only reflection needs to be considered because there is no QD presented. The luminous ambient reflectance R_L of the device is calculated by using Eq. (9). The calculated and simulated luminous ambient reflectance for RGB subpixels are listed in Table 4-1. Due to the reflectance of micro-LED, the luminous ambient reflectance from blue subpixel is dominant.

Table 4-1 Luminous ambient reflectance for RGB subpixels.

Pixels	Red	Green	Blue	RGB	
				Cal.	Sim.
R_L	15.2%	17.0%	26.4%	58.6%	55.0%

4.4DBR for QD-Converted Micro-LED

Besides ambient excitation, another important parameter for QD-converted micro-LED is the optical efficiency, which determines the color performance of the display. Currently, it is still challenging to fabricate QD films with sufficient thickness and conversion efficiency by using existing QD materials and fabrication methods including ink jet printing and photolithography. As a result, the blue micro-LED emission cannot be completely absorbed by QD films and the color gamut is degraded. To solve this issue, some prior arts have proposed to use distributed Bragg reflector (DBR) to enhance the optical efficiency by recycling the blue light [79,101]. However, very few investigations about the ambient light refection by the DBR have been reported.

Figure 4-6 illustrates the system configuration of QD-based micro-LED with DBR. As discussed above, the DBR film reflects the blue light while transmits the green and red lights. Therefore, the blue light can pass through QDs several times to be completely absorbed. We design a wide viewing angle DBR structure with TiO_2/SiO_2 pairs by using commercial thin film coating software TFCalc and its reflectance spectra of DBR structure is shown in Fig. 4-7. As Fig. 4-7 shows, the reflected/transmitted band does not shift even when the angle of incidence increases to 40°.
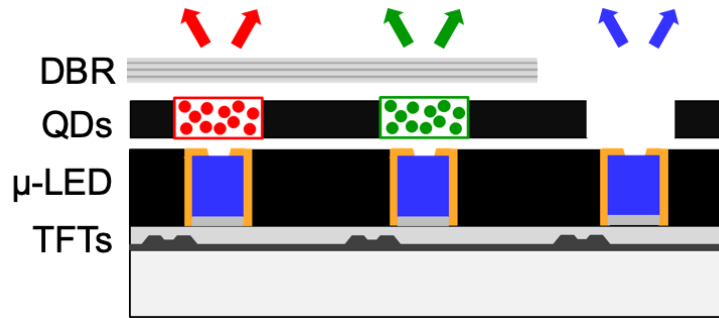
Figure 4-6 Device configuration of QD-converted micro-LED with DBR.
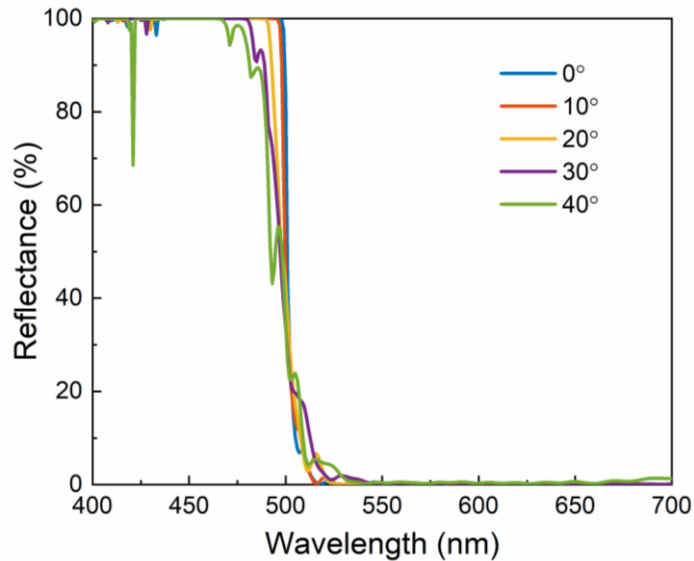
Figure 4-7 Reflectance spectra of the DBR film at different angles of incidence.

To investigate the ambient reflectance of micro-LED display with top DBR, similarly we do the simulation with home-made MATLAB code and LightTools software. Results are plotted in Fig. 4-8 In comparison with the structure without DBR (Fig. 4-4), the ambient reflectance of from DBR increases sharply in the blue range (400~500 nm). Surprisingly, the ambient excitation in the green and red range (500 ~ 700 nm) is still strong even though most of the blue light is reflected by the DBR film. One reason is that the green and red QDs have a broad absorption spectrum from 400 nm to 600 nm as shown in Fig. 4-3, which means they still can be excited to

60

emit green and red lights. Another reason is because although the reflection band of DBR structure is optimized from 0°~40°, part of the blue light at angle of incidence larger than 40° can still pass through the DBR film and be absorbed by the QD particles.
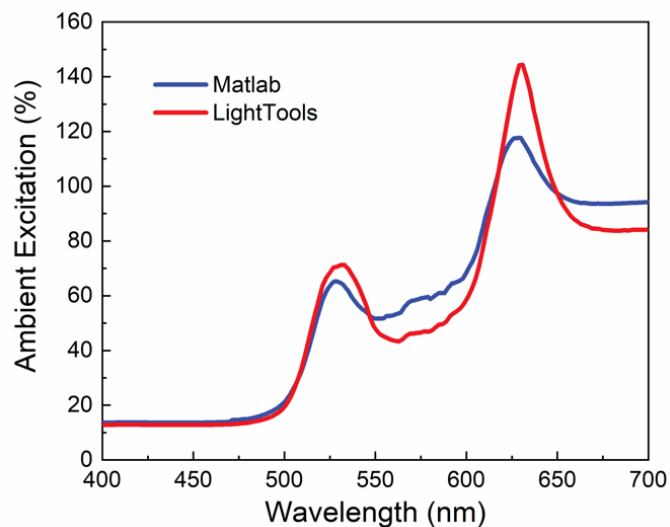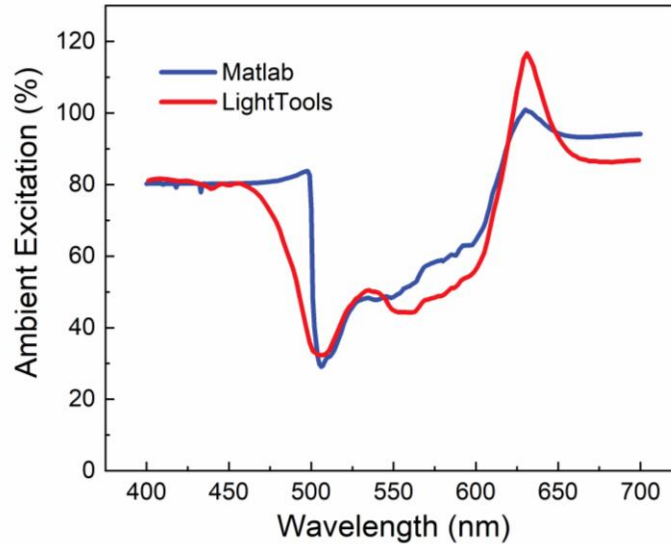

Figure 4-8 Calculated and simulated ambient light excitation spectra in QD-converted micro-LED displays with a DBR film based on Matlab and LightTools.

Figure 4-9 shows the relative ambient reflected spectra for RGB subpixel. Compared to the structure without DBR film, the first-time and second-time excitations are reduced while the reflection increases greatly because of the DBR film, which is consistent with the above discussion. Table 4-2 lists the luminous ambient reflectance for RGB subpixels. The results are very close to those listed in Table 4-1, indicating that DBR film does not help to reduce the ambient reflection.
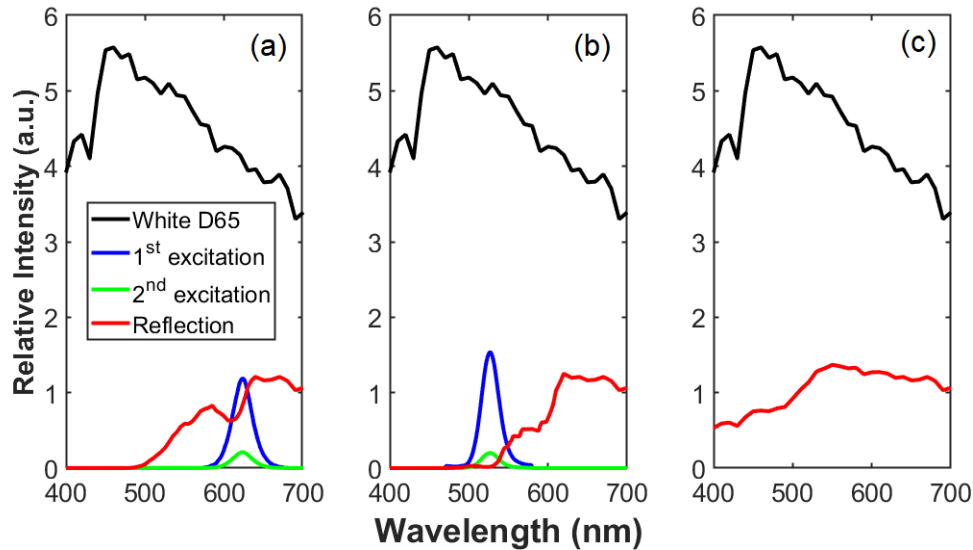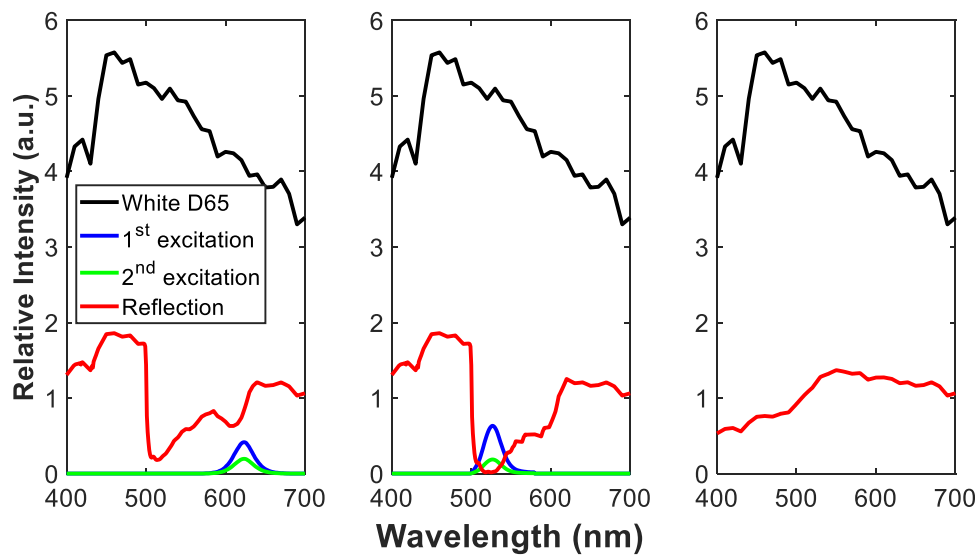
Figure 4-9 Calculated ambient light excitation and reflection for (a) red, (b) green and (c) blue subpixel in QD-converted full color micro-LED displays with a top DBR.

Table 4-2 Luminous ambient reflectance for RGB subpixels with top DBR.

Pixels	Red	Green	Blue	RGB	
				Cal.	Sim.
R_L	16.2%	15.6%	26.4%	58.2%	52.7%

4.5 Color Filter for QD-Converted Micro-LED
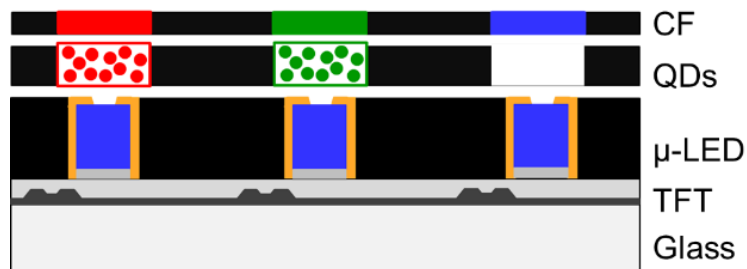
Figure 4-10 Schematic diagram for QD-converted micro-LED with a color filter array.

To improve the display performance and reduce the ambient light excitation from QDs, a layer of RGB color filter is added on top of the QD as shown in Fig. 4-10. The transmission spectra of the color filter are shown in Fig. 4-11 [43]. Figure 4-12 shows the calculated and simulated ambient light excitation spectra. Compared to the results without color filters, the ambient excitation of QDs is greatly suppressed.
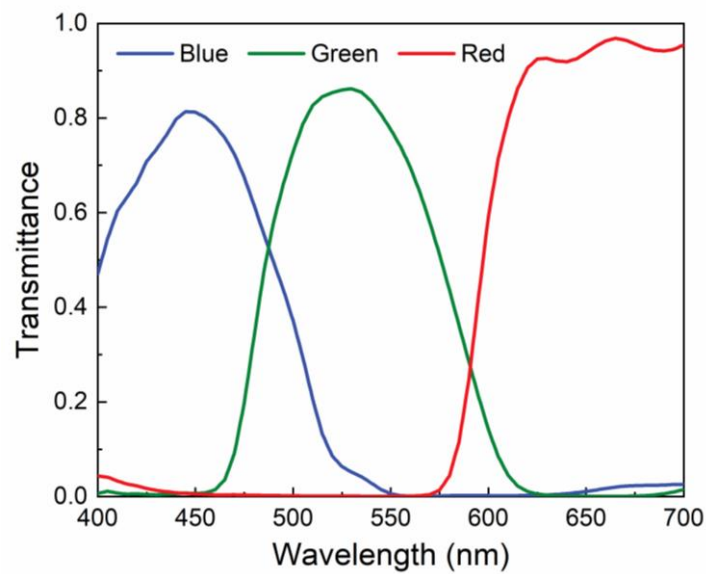
Figure 4-11 Transmittance of RGB color filter [43]**.**
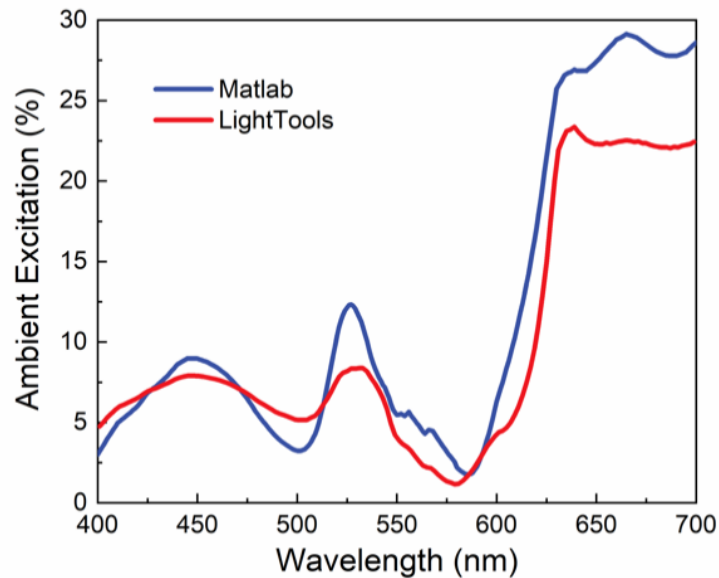
Figure 4-12 Calculated and simulated ambient light excitation spectra in QD-converted micro-LED displays with a top pixelated color filter based on MATLAB and LightTools.

Figure 4-13(a) shows the calculated results for red subpixel, although the reflected red light is still strong, the first-time and second-time excitations are greatly reduced. This is because with the color filters, only the red component in the ambient light can transmit through and enter the QD layer and it can hardly be absorbed according to the absorption spectra in Fig. 4-3. While for green subpixel, because the green QDs can still absorb the green light, the first-time excitation still exists. For the blue subpixel, the blue light is simply reflected by the micro-LEDs and other light is absorbed by the color filter. Table 4-3 lists the luminous ambient reflectance for RGB subpixels. Compared to the results listed in Table 4-1, the reflectance is reduced by ~87% with color filters. Besides, the reflectance from green subpixel is dominant because of human eye sensitivity.
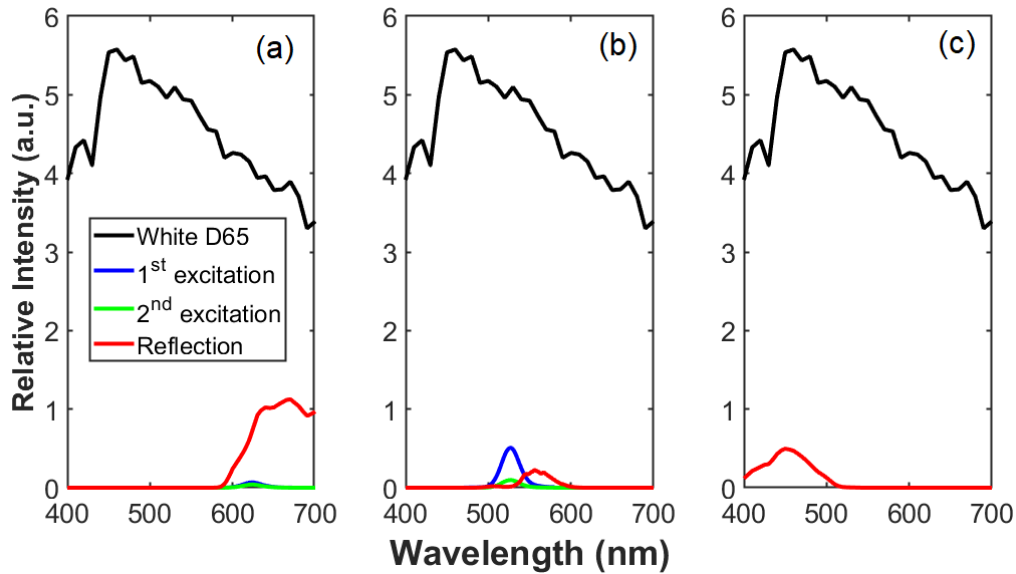
Figure 4-13 Calculated ambient light excitation and reflection for (a) red, (b) green and (c) blue subpixel in QD-converted full color micro-LED displays with top color filter.

Table 4-3 Luminous ambient reflectance for RGB subpixels with top color filter.

Pixels	Red	Green	Blue	RGB	
				Cal.	Sim.
R_L	2.8%	4.4%	0.52%	7.68%	5.8%

In the above ambient light excitation calculation, we assume the area ratio of each subpixel to one pixel is 1/3, which is not practical for real display applications because the black matrix is always needed to reduce the color crosstalk. Therefore, we need to investigate the luminous ambient reflectance as a function of the QD area ratio, which is defined as the QD area to one subpixel area. Besides, the surface reflectance of 1.5% with commercial antireflection coating is applied. Results are plotted in Figure 4-14. As the QD area ratio increases, the luminous ambient

reflectance increases linearly. In addition, the luminous ambient reflectance is greatly suppressed with the top color filter.
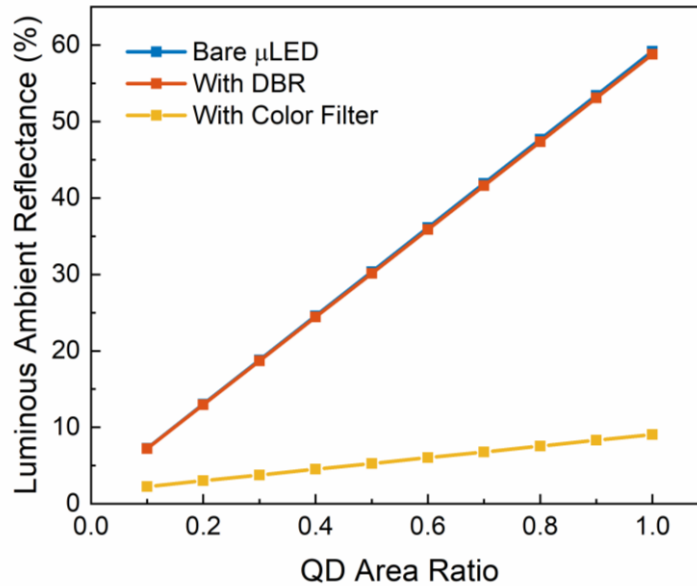
Figure 4-14 Calculated luminous ambient reflectance as a function of QD area ratio. The surface reflectance is 1.5%.

To reduce the ambient reflectance, ambient contrast ratio (ACR) is calculated by using Eq. (10). Figure 4-15 depicts the calculated results at different ambient conditions: office lighting (500 lux), overcast sky (5,000 lux) and full daylight (10,000 lux). The on (off) state luminace L_{on} (L_{off}) are assumed to be 1000 nits (0 nits). The results show that the ACR decreases as the QD area increases because of the increased ambient reflectance. Under the office lighting condition, the ACR of the device without color filter is larger than 10:1 when QD area ratio is smaller than 0.3, which means the display looks great as indicated in Table 3-3 [92]. As the QD area ratio increases to 0.8, the device is still adequately readable (ACR > 5:1). While with the color filter, the ACR becomes much larger than 10:1 even with QD area ratio equal to 1. Under a stronger ambient

lighting condition such as overcast sky as shown in Fig. 4-11(b), the display is barely readable without color filters (ACR ≤ 5:1). But if the QD area is reduced to 0.4, with the help of color filter, the ACR keeps larger than 5:1. However, under full daylight the QD area ratio needs to be further reduced to 0.1 in order to make the display adequately readable. The trade-off is decreased optical efficiency. To address this issue, the employed AR coating can be optimized to reduce the surface reflectance to 0.2% so that the QD area ratio can be kept at 0.3 [91].
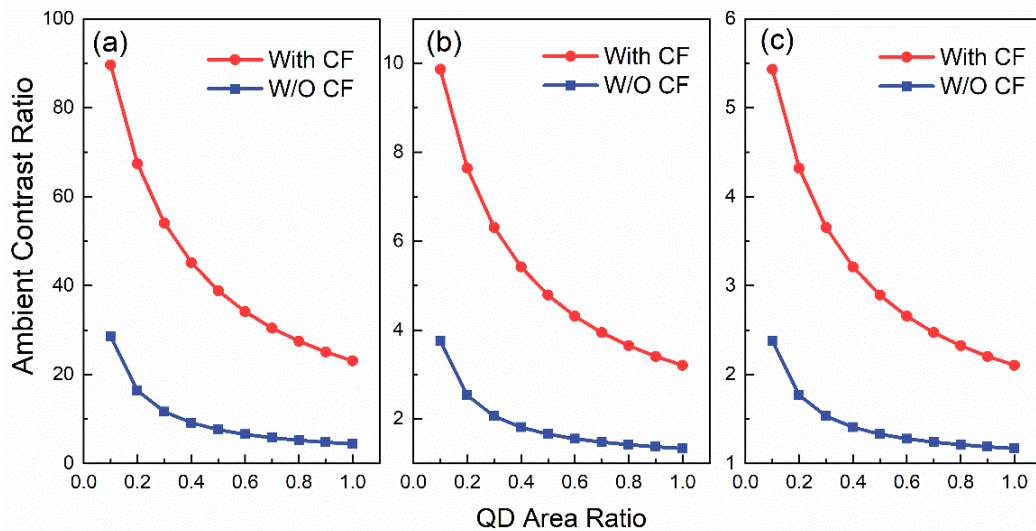
Figure 4-15 Calculated ambient contrast as a function of QD area ratio at ambient light of (a) 500 lux, (b) 5,000 lux and (c) 10,000 lux. The surface reflectance is 1.5%.

4.6 UV Micro-LED with RGB QDs

Figure 4-16 illustrate the layout of UV micro-LEDs with RGB QDs. Compared to blue micro-LEDs with red and green QDs, this device has several advantages: 1) It can balance the RGB colors by adjusting the amount of three QD primaries, leading to better color performance. 2) The viewing angle can be improved because QD particles enable isotropic emission. 3) The angular color shift can be minimized due to matched angular distributions from RGB QDs. 4) The

DBR film optimized for recycling UV light does not need to be patterned, which is more feasible in fabrication. However, the external quantum efficiency (EQE) of UV micro-LED is still much lower than that of blue micro-LED at present.
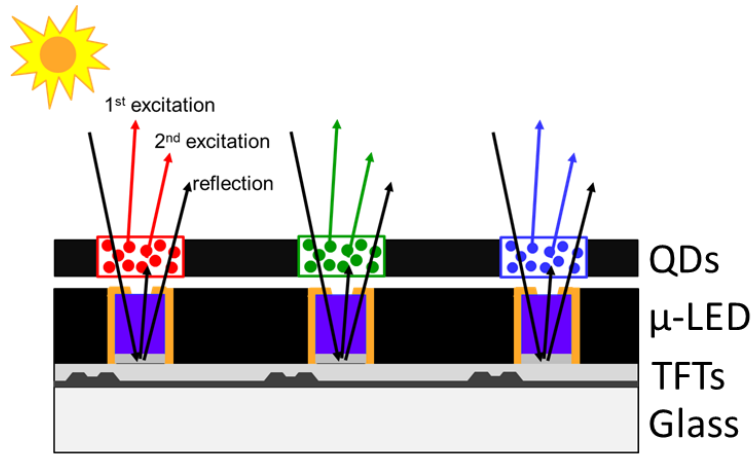
Figure 4-16 Schematic diagram for configuration of UV micro-LED with RGB QDs.

To investigate the ACR of UV micro-LED with RGB QDs, we calculate the luminous ambient reflectance (R_L) and results are listed in Table 4-4. Similar to the results obtained from above sections, the top color filter layer helps to reduce RL of the UV micro-LED device from 58.4% to 7.6%. Figure 4-17 compares the RL of QD-converted UV and blue micro-LED systems with surface reflectance of 1.5%. As expected, these two devices have similar luminous reflectance as the QD ratio changes.

Table 4-4 Luminous ambient reflectance for UV micro-LED with RGB QDs.

Device	Red	Green	Blue	RGB
W/O CF	15.2%	17.0%	26.2%	58.4%
With CF	2.8%	4.3%	0.4%	7.6%
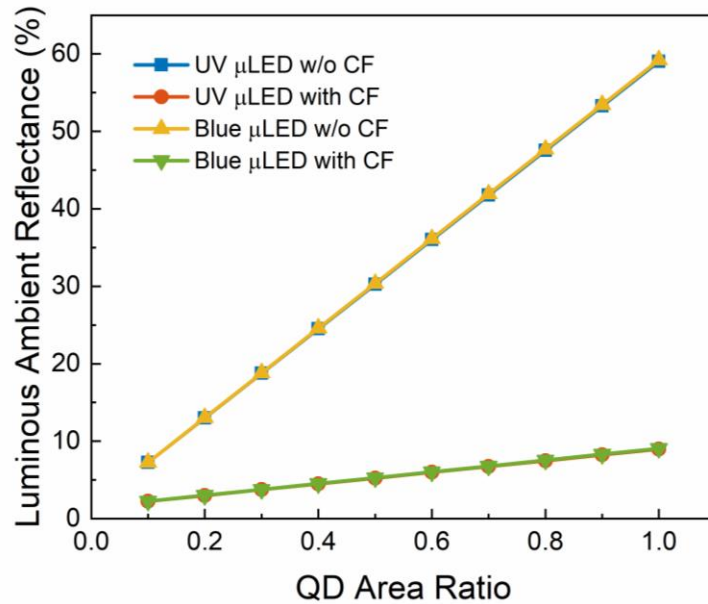
Figure 4-17 Calculated luminous ambient reflectance of UV and blue micro-LED as a function of QD area ratio. The surface reflectance is 1.5%.

4.7 Summary

In this chapter, we mainly discussed the ambient light excitation of QD-converted micro-LED displays. Different from conventional color conversion application in LCD backlight in which QD layer is underneath a stack of optical films, the QDs are on the top surface of micro-LED, which will degrade the ambient contrast ratio of displays. To study this issue quantitatively, we built a simulation model by dividing the ambient excitation into first-time excitation, second-time excitation, and reflection. The luminous ambient reflectance was calculated to be as high as 58.6% for the 100% QD area ratio, indicating a poor ambient contrast ratio. The calculated results agreed very well with the simulated ones based on commercial software LightTools. In addition, a DBR film with wide viewing angle was optimized to enhance the QD conversion efficiency. However, it did not help to improve the ambient contrast ratio. In order to address this issue, a top layer of color filter was employed to absorb the ambient light, which reduced the luminous ambient

reflectance by ~8X. Another method was to reduce the QD area ratio to 0.1 of one subpixel, and the ambient contrast ratio was improved to 5:1 under full daylight, which was adequately readable.

CHAPTER 5 : CONCLUSIONS

In this dissertation, we mainly focus on the challenges of three approaches to form full-color micro-LED displays: 1) individual RGB micro-LED, 2) white micro-LED and 3) quantum dot-converted micro-LED.

For individual RGB micro-LEDs, in order to analyze its angular color shift, we built a simulation model and validated it with experiment. Results show that the sidewall emission causes mismatched angular distributions between AlGaInP-based red micro-LED and InGaN-based blue/green counterparts due to material difference, which further leads to visually noticeable color shift at larger viewing angle. In order to mitigate the color shift while keeping a high light extraction efficiency, a device structure with top black matrix and taper angle in micro-LEDs was proposed. After optimization, the color shift $\Delta u'v'$ of the RGB micro-LED display with 120° taper angle is suppressed to below 0.01 within 80° viewing cone for the first 18 reference colors in Macbeth ColorCheker, and the efficiency keeps ~85% of the device without black matrix. To further improve the efficiency, we proposed microspheres with optimized size on both micro-LED chip and packing resin. For green and blue device, their light extraction efficiencies are enhanced by 54% and 35% respectively. Although only microsphere is discussed in this chapter, microstructure with other shape such as cones or pyramid can be also applied.

For the white micro-LED, we proposed a funnel-tube array to eliminate the color crosstalk. By depositing reflective or absorptive coating on the inner surface of the funnel-tube, a clear boundary was formed between the subpixels to prevent light leakage, thus a near zero optical crosstalk was achieved. To improve the light output efficiency, the taper angle of the funnel-tube

was also optimized. With reflective coating on the inner surface, the light efficiency of the device was enhanced by ~3X as the taper angle [α, β] equals to [76°, 31°]. Compare with the absorptive coating, the ambient contrast ratio with reflective coating is also improved due to higher light intensity despite the increased ambient reflectance. In addition, by utilizing two-color phosphors, which have high thermal stability and resistance to moisture, the color gamut of this device covers 92% of DCI-P3 standard.

For the color-converted micro-LED, we mainly discussed the ambient light excitation of QD. Different from conventional color conversion application in LCD backlight in which QD layer is underneath a stack of optical films, the QDs are on the top surface of micro-LED, which will degrade the ambient contrast ratio of displays. To study this issue quantitatively, we built a simulation model by dividing the ambient excitation into first-time excitation, second-time excitation, and reflection. The luminous ambient reflectance was found to be as high as 58.6% for the 100% QD area ratio, indicating a poor ambient contrast ratio. The calculated results agreed very well with the simulated ones based on commercial software LightTools. In addition, a DBR film with wide viewing angle was optimized to enhance the QD conversion efficiency. However, it did not help to improve the ambient contrast ratio. To address this issue, a top layer of color filter was employed to absorb the ambient light, which reduced the luminous ambient reflectance by ~8X. Another method was to reduce the QD area ratio to 0.1 of one subpixel, and the ambient contrast ratio was improved to 5:1 under the full daylight, which was adequately readable.

APPENDIX: STUDENT PUBLICATIONS

Journal publications

1. E. L. Hsiang, Z. He, Y. Huang, <u>F. Gou</u>, Y. F. Lan, and S.T. Wu, "Improving the power efficiency of micro-LED displays with optimized LED chip sizes," Crystals 10, 494 (2020).

2. L. Wu, <u>F. Gou</u>, S. T. Wu, and Y. Wang, "SLEEPIR: Synchronized Low-Energy Electronically-Chopped PIR Sensor for True Presence Detection," IEEE Sensors Lett. 4(3), 2500204 (2020).

3. Z. He, <u>F. Gou</u>, R. Chen, K. Yin, T. Zhan, and S. T. Wu, "Liquid crystal beam steering devices: principles, recent advances, and future developments," Crystals 9, 292 (2019).

4. <u>F. Gou</u>, E. L. Hsiang, G. Tan, P. T. Chou, Y. L. Li, Y. F. Lan, and S. T. Wu, "Angular color shift of micro-LED displays," Opt. Express (Accepted, 2019).

5. <u>F. Gou</u>, E. L. Hsiang, G. Tan, Y. F. Lan, C. Y. Tsai, and S. T. Wu, "High performance color-converted micro-LED displays," J. Soc. Inf. Display 27, 199-206 (2019).

6. Y. Huang, G. Tan, <u>F. Gou</u>, M. C. Li, S. L. Lee, and S. T. Wu, "Prospects and challenges of mini-LED and micro-LED displays," J. Soc. Inf. Display 27, 387-401 (2019).

7. T. Zhan, Y.H. Lee, G. Tan, J. Xiong, K. Yin, <u>F. Gou</u>, J. Zou, N. Zhang, D. Zhao, J. Yang, S. Liu, and S. T. Wu, "Pancharatnam-Berry optical elements for head-up and near-eye displays," J. Opt. Soc. America B, 36(5), D52-D65 (2019).

8. <u>F. Gou</u>, E. L. Hsiang, G. Tan, Y. F. Lan, C. Y. Tsai, and Shin-Tson Wu, "Tripping the optical efficiency of color-converted micro-LED display with funnel-tube array," Crystals, 9(1), 39 (2019).

9. F. Gou, R. Chen, M. Hu, J. Li, J. Li, Z. An, and S. T. Wu, "Submillisecond-response polymer network liquid crystals for mid-infrared applications," Opt. Express 26(23), 29735-29743 (2018).

10. F. Gou, H. Chen, M.C. Li, S.L. Lee, and S. T. Wu, "Motion-blur-free LCD for high resolution virtual reality displays," J. Soc. Inf. Display 26(4), 223-228 (2018).

11. G. G. Liu, K. Wang, Y. H. Lee, D. Wang, P. P. Li, F. Gou, Y. Li, C. Tu, S. T. Wu, and H. T. Wang, "Measurement of the topological charge and index of vortex vector optical fields with a space-variant half-wave plate," Opt. Lett. 43(4), 823-826 (2018).

12. Y. H. Lee, D. Franklin, F. Gou, G. Liu, F. Peng, D. Chanda, and S. T. Wu, "Two-photon polymerization enabled multi-layer liquid crystal phase modulator," Sci. Rep. 7, 16260 (2017).

13. F. Gou, F. Peng, Q. Ru, Y. H. Lee, H. Chen, Z. He, T. Zhan, K. L. Vodopyanov, and S. T. Wu, "Mid-wave infrared beam steering based on high-efficiency liquid crystal diffractive waveplates," Opt. Express 25(19), 22404-22410 (2017).

14. G. Tan, Y. H. Lee, F. Gou, H. Chen, Y. Huang, Y.F. Lan, C.Y. Tsai, and S. T. Wu, "Review on Polymer-Stabilized Short-Pitch Cholesteric Liquid Crystal Displays," J. Phys. D: Appl. Phys. 50, 493001 (2017).

15. Z. He, Y. H. Lee, F. Gou, D. Franklin, D. Chanda, and S. T. Wu, "Polarization-independent phase modulators enabled by two-photon polymerization," Opt. Express 25(26), 33688-33694 (2017).

16. Y. H. Lee, G. Tan, T. Zhan, Y. Weng, G. Liu, F. Gou, F. Peng, N.V. Tabiryan, S. Gauza, and S. T. Wu, "Recent progress in Pancharatnam-Berry phase optical elements and the

applications for virtual/augmented realities," Optical Data Processing and Storage 3(1), 79-88 (2017).

17. G. Tan, Y. H. Lee, F. Gou, M. Hu, Y. F. Lan, C. Y. Tsai, and S. T. Wu, "Macroscopic model for analyzing the electro-optics of uniform lying helix cholesteric liquid crystals," J. Appl. Phys. 121(17), 173102 (2017).

18. F. Gou, H. Chen, M. C. Li, S. L. Lee, and S. T. Wu, "Submillisecond-response liquid crystal for high-resolution virtual reality displays," Opt. Express 25(7), 7984-7997 (2017).

19. F. Peng, H. Chen, F. Gou, Y. H. Lee, M. Wand, M.C. Li, S.L. Lee, and S. T. Wu, "Analytical equation for the motion picture response time of display devices," J. Appl. Phys. 121(2), 023108 (2017).

20. H. Chen, F. Gou, and S. T. Wu, "A submillisecond-response nematic liquid crystal for augmented reality displays," Opt. Mater. Express 7(1), 195-201 (2017).

21. H. Chen, F. Peng, F. Gou, Y. H. Lee, M. Wand, and S. T. Wu, "Nematic LCD with motion picture response time comparable to organic LEDs," Optica 3(9), 1033-1034 (2016).

22. Y. H. Lee, F. Gou, F. Peng, and S.T. Wu, "Hysteresis-free and submillisecond-response polymer network liquid crystal," Opt. Express 24(13) 14793-14800 (2016).

23. F. Peng, F. Gou, H. Chen, Y. Huang, and S. T. Wu, "A submillisecond-response liquid crystal for color sequential projection displays," J. SID 24(4), 241-245 (2016).

24. F. Peng, Y. Huang, F. Gou, M. Hu, J. Li, Z. An, and S. T. Wu, "High performance liquid crystals for vehicle displays," Opt. Mater. Express 6(3), 717-726 (2016).

Conference proceedings

1. F. Gou, E. L. Hsiang, G. Tan, P. T. Chou, Y. L. Li, Y. F. Lan, and S. T. Wu, "High-efficiency micro-LED displays with indistinguishable color shift," Proc. SPIE 11304, 113040I (February 2020, San Francisco, California).

2. F. Gou, E. L. Hsiang, G. Tan, Y. F. Lan, C. Y. Tsai, and S. T. Wu, "High performance color-converted micro-LED displays," SID Symp. Digest 50(1), 22-25 (May 2019, San Jose, California).

3. F. Gou, H. Chen, M.C. Li, S. L. Lee, and S.T. Wu, "Blur-free LCD for high resolution virtual reality displays," SID Symp. Digest 49(1), 577-580 (May 2018, Los Angeles, California).

4. F. Gou, Y. H. Lee, G. Tan, M. Hu, Y. F. Lan, C. Y. Tsai, and S. T. Wu, "Submillisecond grayscale response time of a uniform lying helix liquid crystal," SID Symp. Digest 48(1), 1822-1825 (May 2017, Los Angeles, California).

5. G. Tan, Y. H. Lee, F. Gou, M. Hu, Y.-F. Lan, C.-Y. Tsai, and S. T. Wu, "Figure of Merit for Optimizing the Performance of Uniform Lying Helix Cholesteric Liquid Crystals," SID Symp. Digest 48(1), 490-493 (May 2017, Los Angeles, California).

6. F. Peng, H. Chen, F. Gou, Y. H. Lee, S. T. Wu, M. Wand, M. C. Li, and S. L. Lee, "A LCD with submillisecond motion picture response time," SID Symp. Digest 48(1), 1826-1829 (May 2017, Los Angeles, California).

7. H. Chen, F. Gou, and S. T. Wu, "Submillisecond-response nematic LC for wearable displays," SID Symp. Digest 48(1), 377-380 (May 2017, Los Angeles, California).

8. H. Chen, F. Peng, F. Gou, M. Wand, and S. T. Wu, "Fast-response LCDs for virtual reality applications," Proc. SPIE 10125, 101251E (February 2017).

9. F. Peng, H. Chen, F. Gou, Y. Huang, and S. T. Wu, "A submillisecond-response liquid crystal for color-sequential projection displays," SID Symp. Digest 47(1), 1025-1028 (May 2016, San Francisco, California).

10. F. Peng, Y. Huang, F. Gou, S. T. Wu, M. Hu, J. Li, and Z. An, "High-performance liquid crystals for vehicular displays," SID Symp. Digest 47(1) 754-756 (May 2016, San Francisco, California).

<div align="center">Patents</div>

1. Y. H. Lee, T. Zhan, G. Tan, F. Gou, F. Peng, S. T. Wu, "Optical Display System with Enhanced Resolution, Methods, and Applications," US Patent 10,115,327 B1 (Oct. 30, 2018).

REFERENCES

1.   S. Pimputkar, J. S. Speck, S. P. Denbaars, and S. Nakamura, "Prospects for LED lighting," Nat. Photonics **3**, 180–182 (2009).

2.   G. Murtaza and J. . Senior, "Method for extracting thermally stable optical signals from a GaAlAs LED source," IEEE Photonics Technol. Lett. **7**, 479–481 (1995).

3.   T. Komine and M. N. Consumer, "Fundamental analysis for visible-light communication system using LED lights," IEEE Trans. Consum. Electron. **50**, 100–107 (2004).

4.   H. Chun, S. Rajbhandari, G. Faulkner, D. Tsonev, E. Xie, J. J. D. McKendry, E. Gu, M. D. Dawson, D. C. O'Brien, and H. Haas, "LED based wavelength division multiplexed 10 Gb/s visible light communications," J. Light. Technol. **34**, 3047–3052 (2016).

5.   L Svilainis, "LED brightness control for video display application," Displays **29**, 506–511 (2008).

6.   H. Yamamoto, M. Kouno, S. Muguruma, Y. Hayasaki, Y. Nagai, Y. Shimizu, and N. Nishida, "Enlargement of viewing area of stereoscopic full-color LED display by use of a parallax barrier," Appl. Opt. **41**, 6907 (2002).

7.   C. C. Chen, C. Y. Wu, Y. M. Chen, and T. F. Wu, "Sequential color LED backlight driving system for LCD panels," IEEE Trans. Power Electron. **22**, 919–925 (2007).

8.   M. Schadt, "Milestone in the history of field-effect liquid crystal displays and materials related content," Jpn. J. Appl. Phys. **48**, 1–9 (2009).

9.   G. Tan, Y. Huang, M.-C. Li, S.-L. Lee, and S.-T. Wu, "High dynamic range liquid crystal displays with a mini-LED backlight," Opt. Express **26**, 16572–16584 (2018).

10.   Y. Huang, G. Tan, F. Gou, M.-C. Li, S.-L. Lee, and S.-T. Wu, "Prospects and challenges

of mini-LED and micro-LED displays," J. Soc. Inf. Disp. **27**, 387–401 (2019).

11.   H. F. Chen, T. H. Ha, J. H. Sung, H. R. Kim, and B. H. Han, "Evaluation of LCD local-dimming-backlight system," J. Soc. Inf. Disp. **18**, 57–65 (2010).

12.   P. de Greef and H. G. Hulze, "Adaptive dimming and boosting backlight for LCD-TV systems," SID Int. Symp. Dig. Tech. Pap. **38**, 1332–1335 (2007).

13.   H. Chen, T. H. Ha, J. H. Sung, H. R. Kim, and B. H. Han, "Evaluation of LCD local-dimming-backlight system," J. Soc. Inf. Disp. **18**, 57 (2010).

14.   S. X. Jin, J. Li, J. Z. Li, J. Y. Lin, and H. X. Jiang, "GaN microdisk light emitting diodes," Appl. Phys. Lett. **76**, 631 (2000).

15.   H. X. Jiang and J. Y. Lin, "Nitride micro-LEDs and beyond - a decade progress review," Opt. Express **21**, A475 (2013).

16.   Z. Liu, W. C. Chong, K. M. Wong, and K. M. Lau, "GaN-based LED micro-displays for wearable applications," Microelectron. Eng. **148**, 98–103 (2015).

17.   C. W. Tang and S. A. Vanslyke, "Organic electroluminescent diodes," Appl. Phys. Lett. **51**, 913–915 (1987).

18.   Z. Luo, Y. Chen, and S.-T. Wu, "Wide color gamut LCD with a quantum dot backlight," Opt. Express **21**, 26269 (2013).

19.   H. W. Chen, R. D. Zhu, J. He, W. Duan, W. Hu, Y. Q. Lu, M. C. Li, S. L. Lee, Y. J. Dong, and S. T. Wu, "Going beyond the limit of an LCD's color gamut," Light Sci. Appl. **6**, e17043–e17043 (2017).

20.   H. Chen, F. Gou, and S.-T. Wu, "Submillisecond-response nematic liquid crystals for augmented reality displays," Opt. Mater. Express **7**, 1076–1079 (2017).

21.   F. Gou, H. Chen, M.-C. Li, S.-L. Lee, and S.-T. Wu, "Submillisecond-response liquid crystal for high-resolution virtual reality displays," Opt. Express **25**, 7984–7997 (2017).

22.   T. Wu, C.-W. Sher, Y. Lin, C.-F. Lee, S. Liang, Y. Lu, S.-W. Huang Chen, W. Guo, H.-C. Kuo, and Z. Chen, "Mini-LED and Micro-LED: promising candidates for the next generation display technology," Appl. Sci. **8**, 1557 (2018).

23.   E. H. Virey, N. Baron, Y. Developpement, and S. Antipolis, "Status and Prospects of microLED Displays," SID Int. Symp. Dig. Tech. Pap. **49**, 593–596 (2018).

24.   V. W. Lee, N. Twu, and I. Kymissis, "Micro-LED technologies and applications," Inf. Disp. (1975). **32**, 16–23 (2016).

25.   F. Peng, H. Chen, F. Gou, Y.-H. Lee, M. Wand, M.-C. Li, S.-L. Lee, and S.-T. Wu, "Analytical equation for the motion picture response time of display devices," J. Appl. Phys. **121**, 023108 (2017).

26.   H. Chen, F. Peng, F. Gou, Y.-H. Lee, M. Wand, and S.-T. Wu, "Nematic LCD with motion picture response time comparable to organic LEDs," Optica **3**, 1033–1034 (2016).

27.   S. S. Konoplev, K. A. Bulashevich, and S. Y. Karpov, "From large-size to micro-LEDs: scaling trends revealed by modeling," Phys. Status Solidi Appl. Mater. Sci. **215**, 1–6 (2018).

28.   H. W. Choi, C. W. Jeon, M. D. Dawson, P. R. Edwards, R. W. Martin, and S. Tripathy, "Mechanism of enhanced light output efficiency in InGaN-based microlight emitting diodes," J. Appl. Phys. **93**, 5978–5982 (2003).

29.   G. Biwa, M. Doi, A. Yasuda, and H. Kadota, "The technologies for Crystal LED display system in each pixel," SID Int. Symp. Dig. Tech. Pap. **50**, 121–124 (2019).

30.   N. Sugiura, C. Chuang, C. Hsieh, C. Wu, C. Tsai, C. Lin, C. Liu, C. Liu, C. Yeh, C. Liu,

and Y. Lin, "12.1-inch 169-ppi full-color micro-LED display using LTPS-TFT backplane," SID Int. Symp. Dig. Tech. Pap. **50**, 450–453 (2019).

31. Y. Liu, K. Liao, C. Lin, and Y. Li, "PixeLED display for transparent applications," SID Int. Symp. Dig. Tech. Pap. **49**, 874–875 (2018).

32. R. S. Cok, M. Meitl, R. Rotzoll, G. Melnik, A. Fecioru, A. J. Trindade, B. Raymond, S. Bonafede, D. Gomez, T. Moore, C. Prevatte, E. Radauscher, S. Goodwin, P. Hines, and C. A. Bower, "Inorganic light-emitting diode displays using micro-transfer printing," J. Soc. Inf. Disp. **25**, 589–609 (2017).

33. A. Paranjpe, J. Montgomery, S. M. Lee, and C. Morath, "Micro-LED displays : key manufacturing challenges and solutions," SID Int. Symp. Dig. Tech. Pap. **49**, 597–600 (2018).

34. M. A. Meitl, Z. T. Zhu, V. Kumar, K. J. Lee, X. Feng, Y. Y. Huang, I. Adesida, R. G. Nuzzo, and J. A. Rogers, "Transfer printing by kinetic control of adhesion to an elastomeric stamp," Nat. Mater. **5**, 33–38 (2006).

35. S. H. Ahn and L. J. Guo, "Large-area roll-to-roll and roll-to-plate Nanoimprint Lithography: A step toward high-throughput application of continuous nanoimprinting," ACS Nano **3**, 2304–2310 (2009).

36. F. J. Henley, "Combining engineered EPI growth substrate materials with novel test and mass-transfer equipment to enable microLED mass-Production," SID Int. Symp. Dig. Tech. Pap. **49**, 688–691 (2018).

37. K. Tsuchiyama, K. Yamane, H. Sekiguchi, H. Okada, and A. Wakahara, "Fabrication of Si/SiO2/GaN structure by surface-activated bonding for monolithic integration of

optoelectronic devices," Jpn. J. Appl. Phys. **55**, 05FL01 (2016).

38. K. Tsuchiyama, K. Yamane, S. Utsunomiya, H. Sekiguchi, H. Okada, and A. Wakahara, "Monolithic integration of Si-MOSFET and GaN-LED using Si/SiO2/GaN-LED wafer," Appl. Phys. Express **9**, 104101 (2016).

39. Z. J. Liu, K. M. Wong, C. W. Keung, C. W. Tang, and K. M. Lau, "Monolithic LED microdisplay on active matrix substrate using flip-chip technology," IEEE J. Sel. Top. Quantum Electron. **15**, 1298–1302 (2009).

40. K. Ding, V. Avrutin, N. Izyumskaya, Ü. Özgür, and H. Morkoç, "Micro-LEDs, a manufacturability perspective," Appl. Sci. **9**, 1206 (2019).

41. F. Lu, D. Lee, D. Byrnes, E. Armour, and W. Quinn, "Blue LED growth from 2 inch to 8 inch," Sci. China Technol. Sci. **54**, 33–37 (2011).

42. A. Beckers, D. Fahle, C. Mauder, T. Kruecken, A. R. Boyd, and M. Heuken, "Enabling the next era of display technologies by micro LED MOCVD processing," SID Int. Symp. Dig. Tech. Pap. **49**, 601–603 (2018).

43. F. Gou, E.-L. Hsiang, G. Tan, Y.-F. Lan, C.-Y. Tsai, and S.-T. Wu, "Tripling the pptical efficiency of color-converted micro-LED displays with funnel-tube array," Crystals **9**, 39 (2019).

44. F. Gou, E. Hsiang, G. Tan, Y. Lan, C. Tsai, and S. Wu, "High performance color-converted micro-LED displays," J. Soc. Inf. Disp. **27**, 199–206 (2019).

45. H.-Y. Lin, C.-W. Sher, D.-H. Hsieh, X.-Y. Chen, H.-M. P. Chen, T.-M. Chen, K.-M. Lau, C.-H. Chen, C.-C. Lin, and H.-C. Kuo, "Optical cross-talk reduction in a quantum-dot-based full-color micro-light-emitting-diode display by a lithographic-fabricated photoresist

mold," Photonics Res. **5**, 411 (2017).

46. H.-V. Han, H.-Y. Lin, C.-C. Lin, W.-C. Chong, J.-R. Li, K.-J. Chen, P. Yu, T.-M. Chen, H.-M. Chen, K.-M. Lau, and H.-C. Kuo, "Resonant-enhanced full-color emission of quantum-dot-based micro LED display technology," Opt. Express **23**, 32504 (2015).

47. R. W. Martin, M. D. Dawson, H. W. Choi, C. W. Jeon, P. R. Edwards, and S. Tripathy, "Mechanism of enhanced light output efficiency in InGaN-based microlight emitting diodes," J. Appl. Phys. **93**, 5978–5982 (2003).

48. F. Olivier, A. Daami, C. Licitra, and F. Templier, "Shockley-Read-Hall and Auger non-radiative recombination in GaN based LEDs: A size effect study," Appl. Phys. Lett. **111**, 22101–22104 (2017).

49. X. H. Wang, W. Y. Fu, P. T. Lai, and H. W. Choi, "Evaluation of InGaN / GaN light-emitting diodes of circular geometry," Opt. Express **17**, 22311–22319 (2009).

50. L. Zhang, F. Ou, W. C. Chong, Y. Chen, and Q. Li, "Wafer-scale monolithic hybrid integration of Si-based IC and III-V epi-layers-A mass manufacturable approach for active matrix micro-LED micro-displays," J. Soc. Inf. Disp. **26**, 786–789 (2018).

51. M. S. Wong, C. Lee, D. J. Myers, D. Hwang, J. A. Kearns, T. Li, J. S. Speck, S. Nakamura, and S. P. DenBaars, "Size-independent peak efficiency of III-nitride micro-light-emitting-diodes using chemical treatment and sidewall passivation," Appl. Phys. Express **12**, 1–4 (2019).

52. M. R. Krames, O. B. Shchekin, R. Mueller-Mach, G. O. Mueller, L. Zhou, G. Harbers, and M. G. Craford, "Status and future of high-power light-emitting diodes for solid-state lighting," IEEE/OSA J. Disp. Technol. **3**, 160–175 (2007).

53.	G. A. Melnik, D. Gomez, B. Raymond, R. Cok, M. A. Meitl, A. J. Trindade, E. Radauscher, T. Moore, B. Fisher, C. Prevatte, C. A. Bower, A. Fecioru, R. Rotzoll, and S. Bonafede, "Emissive displays with transfer-printed assemblies of 8 μm × 15 μm inorganic light-emitting diodes," Photonics Res. **5**, A23 (2017).

54.	G. Tan, J.-H. Lee, S.-C. Lin, R. Zhu, S.-H. Choi, and S.-T. Wu, "Analysis and optimization on the angular color shift of RGB OLED displays," Opt. Express **25**, 33629 (2017).

55.	E. Jang, S. Jun, H. Jang, J. Lim, B. Kim, and Y. Kim, "White-light-emitting diodes with quantum dot color converters for display backlights," Adv. Mater. **22**, 3076–3080 (2010).

56.	H. Chen, J. He, and S. Wu, "Recent advances on quantum-dot-enhanced liquid-crystal displays," IEEE J. Sel. Top. Quantum Electron. **23**, 1900611 (2017).

57.	R. Zhu, Z. Luo, H. Chen, Y. Dong, and S.-T. Wu, "Realizing Rec 2020 color gamut with quantum dot displays," Opt. Express **23**, 23680 (2015).

58.	Z. Zhao, X. Wang, K. Yang, F. Fan, D. Wu, S. Liu, and K. Wang, "Analysis of factors affecting optical performance of GaN-based micro-LEDs with quantum dots films," Crystals **10**, 203 (2020).

59.	S. Nakamura and M. R. Krames, "History of gallium-nitride-based light-emitting diodes for illumination," Proc. IEEE **101**, 2211–2220 (2013).

60.	C. A. Hurni, A. David, M. J. Cich, R. I. Aldaz, B. Ellis, K. Huang, A. Tyagi, R. A. Delille, M. D. Craven, F. M. Steranka, and M. R. Krames, "Bulk GaN flip-chip violet light-emitting diodes with optimized efficiency for high-power operation," Appl. Phys. Lett. **106**, 031101 (2015).

61.	R. H. Horng, H. Y. Chien, K. Y. Chen, W. Y. Tseng, Y. T. Tsai, and F. G. Tarntair,

"Development and fabrication of AlGaInP-based flip-chip micro-LEDs," IEEE J. Electron Devices Soc. **6**, 475–479 (2018).

62. W. Chen, G. Hu, J. Lin, J. Jiang, M. Liu, Y. Yang, G. Hu, Y. Lin, Z. Wu, Y. Liu, and B. Zhang, "High-performance, single-pyramid micro light-emitting diode with leakage current confinement layer," Appl. Phys. Express **8**, 032102 (2015).

63. F. Olivier, S. Tirano, L. Dupré, B. Aventurier, C. Largeron, and F. Templier, "Influence of size-reduction on the performances of GaN-based micro-LEDs for display application," J. Lumin. **191**, 112–116 (2017).

64. Z. Liu, K. Wang, X. Luo, and S. Liu, "Precise optical modeling of blue light-emitting diodes by Monte Carlo ray-tracing," Opt. Express **18**, 9398 (2010).

65. M. Moser, R. Winterhoff, C. Geng, I. Queisser, F. Scholz, and A. Dörnen, "Refractive index of (AlxGa1−x)0.5In0.5P grown by metalorganic vapor phase epitaxy," Appl. Phys. Lett **64**, 235 (1994).

66. S. J. Lee, "Analysis of light-emitting diodes by Monte Carlo photon simulation," Appl. Opt. **40**, 1427 (2007).

67. R. Hunt and M. Pointer, *Measuring Colour*, 4th ed. (John Wiley & Sons, 2011).

68. M. D. Fairchild, *Color Appearance Models*, 3rd ed. (Wiley, 2013).

69. Y. D. Qi, H. Liang, D. Wang, Z. D. Lu, W. Tang, and K. M. Lau, "Comparison of blue and green InGaNGaN multiple-quantum-well light-emitting diodes grown by metalorganic vapor phase epitaxy," Appl. Phys. Lett. **86**, 1–3 (2005).

70. J. Lee, J. Lee, S. Kim, H. J.-I. transactions on Electron, and U. 2008, "GaN light-emitting diode with deep-angled mesa sidewalls for enhanced light emission in the surface-normal

direction," IEEE Trans. Electron Dev. **55**, 523–526 (2008).

71. C. Kao, H. Kuo, H. Huang, J. Chu, Y. Peng, Y. Hsieh, C. Y. Luo, S. Wang, C. Yu, and C. Lin, "Light-output enhancement in a nitride-based light-emitting diode with 22 undercut sidewalls," IEEE Photonics Technol. Lett. **17**, 22–24 (2005).

72. K. Tomoda, N. Hirao, and G. Biwa, "Light emitting unit and display device," U.S. patent 8686447 B2 (2014).

73. C. McCamy, H. Marcus, and J. G. Davidson, "A color-rendition chart," J. App. Photog. Eng. **2**, 95–99 (1976).

74. J. A. Dobrowolski, B. T. Sullivan, and R. C. Bajcar, "Optical interference, contrast-enhanced electroluminescent device," Appl. Opt. **31**, 5988 (1992).

75. A. Ohmae, Y. Kataoka, I. Nishinaka, T. Ohashi, G. Sakoda, and G. Biwa, "Light emitting apparatus, light emitting unit, display apparatus, electronic device and light emitting element," U.S. patent 10168004 B2 (2019).

76. B. Pyo, C. Joo, H. Kim, B. Kwon, J. Lee, J. Lee, and M. C. Suh, "A nanoporous polymer film as a diffuser as well as a light extraction component for top emitting organic light emitting diodes with a strong microcavity structure," Nanoscale **8**, 8575–8582 (2016).

77. S. J. Lee and S. W. Song, "Efficiency improvement in light-emitting diodes based on geometrically deformed chips," Light. Diodes Res. Manuf. Appl. III **3621**, 237–248 (2003).

78. X. Ding, Y. Tang, Z. Li, J. Li, Y. Xie, and L. Lin, "Multichip LED modules with V-groove surfaces for light extraction efficiency enhancements considering roughness scattering," IEEE Trans. Electron Devices **64**, 182–188 (2017).

79. G. Chen, B. Wei, C. Lee, and H. Lee, "Monolithic Red/Green blue micro-LEDs with HBR

and DBR structures," IEEE Photonics Technol. Lett. **30**, 262–265 (2018).

80. M. Zollers, *Phosphor Modeling in LightTools* (2011).

81. N. T. Tran, F. G. Shi, and J. P. You, "Effect of phosphor particle dize on luminous efficacy of phosphor-converted white LED," J. Light. Technol. **27**, 5145–5150 (2009).

82. W. Centre, G. R. Fern, P. G. Harris, T. G. Ireland, and J. Silver, "Sub-micrometre phosphor preparation for next generation displays," SID Int. Symp. Dig. Tech. Pap. **48**, 1711–1714 (2017).

83. H. Hulst and H. van de Hulst, *Light Scattering by Small Particles* (Wiley, 1981).

84. D. C. Chen, Z. G. Liu, Z. H. Deng, C. Wang, Y. G. Cao, and Q. L. Liu, "Optimization of light efficacy and angular color uniformity by hybrid phosphor particle size for white light-emitting diode," Rare Met. **33**, 348–352 (2014).

85. J. Silver, P. Harris, G. Fern, J. Bonar, G. Valentine, and S. Gorton, "Novel approach to the manufacture of microLED colour conversion structures," in *International Displays Workshop* (2016), pp. 1183–1186.

86. L. Wang, X. Wang, T. Kohsei, K. Yoshimura, M. Izumi, N. Hirosaki, and R.-J. Xie, "Highly efficient narrow-band green and red phosphors enabling wider color-gamut LED backlight for more brilliant displays," Opt. Express **23**, 28707 (2015).

87. SMPTE RP, *D-Cinema Quality—Reference Projector and Environment* (2011).

88. B. Series, *Parameter Values for Ultra-High Definition Television Systems for Production and International Programme Exchange BT Series Broadcasting Service (Television)* (2012).

89. K. Masaoka, Y. Nishida, Sugawara.M, and E. Nakasu, "Design of primaries for a wide-

gamut television colorimetry," IEEE Trans. Broadcast **56**, 452–457 (2010).

90. R. Singh, K. N. Narayanan Unni, A. Solanki, and Deepak, "Improving the contrast ratio of OLED displays: An analysis of various techniques," Opt. Mater. (Amst). **34**, 716–723 (2012).

91. G. Tan, J.-H. Lee, Y.-H. Lan, M.-K. Wei, L.-H. Peng, I.-C. Cheng, and S.-T. Wu, "Broadband antireflection film with moth-eye-like structure for flexible display applications," Optica **4**, 678 (2017).

92. G. Walker, "GD-Itronix Dynavue Technology: The ultimate outdoor-readable touch-screen display," Rugged PC Rev. (2007).

93. Y. Shirasaki, G. J. Supran, M. G. Bawendi, and V. Bulović, "Emergence of colloidal quantum-dot light-emitting technologies," Nat. Photonics **7**, 13–23 (2013).

94. J. S. Steckel, R. Colby, W. Liu, K. Hutchinson, C. Breen, J. Ritter, and S. Coe-Sullivan, "Quantum dot manufacturing requirements for the high volume LCD market," SID Int. Symp. Dig. Tech. Pap. **44**, 943–945 (2013).

95. Z. Luo, D. Xu, and S. Wu, "Emerging quantum-dots-enhanced LCDs," J. Disp. Technol. **10**, 526–539 (2014).

96. A. M. Smith and S. Nie, "Semiconductor nanocrystals: Structure, properties, and band gap engineering," Acc. Chem. Res. **43**, 190–200 (2010).

97. Z. Liu, C. H. Lin, B. R. Hyun, C. W. Sher, Z. Lv, B. Luo, F. Jiang, T. Wu, C. H. Ho, H. C. Kuo, and J. H. He, "Micro-light-emitting diodes with quantum dots in display technology," Light Sci. Appl. **9**, 83 (2020).

98. C. J. Chen, J. Y. Lien, S. L. Wang, and R. K. Chiang, "Thick-shelled quantum dots for

display applications," SID Int. Symp. Dig. Tech. Pap. **48**, 550–553 (2017).

99. M.-H. Shin, H.-J. Kim, and Y.-J. Kim, "Optical modeling based on mean free path calculations for quantum dot phosphors applied to optoelectronic devices," Opt. Express **25**, A113 (2017).

100. Q. Hong, K.-C. Lee, Z. Luo, and S.-T. Wu, "High-efficiency quantum dot remote phosphor film," Appl. Opt. **54**, 4617–4622 (2015).

101. C. Lee, C. Cheng, H. Lee, Y. Chu, Y. Fang, C. Chao, and M. Wu, "Color conversion of GaN-based micro light-emitting diodes using quantum dots," IEEE Photonics Technol. Lett. **27**, 2296–2299 (2015).